UNIVERSITY OF CALIFORNIA,
IRVINE

Integrated Stretchable Electronics for Human Vital Signs Monitoring

DISSERTATION

submitted in partial satisfaction of the requirements
for the degree of

DOCTOR OF PHILOSOPHY

in Biomedical Engineering

by

Michael Chu

Dissertation Committee:
Professor Michelle Khine, Chair
Professor Zoran Nenadic
Professor William Tang

2019

DEDICATION

To:

My friends and family for their continual support and encouragement through this journey

TABLE OF CONTENTS

	Page
LIST OF FIGURES	iv
LIST OF TABLES	v
ACKNOWLEDGMENTS	vi
CURRICULUM VITAE	vii
ABSTRACT OF THE DISSERTATION	viii
INTRODUCTION	1
CHAPTER 2: Signals from the Human Body	4
CHAPTER 3: Soft Electronics Requirements and Background	16
CHAPTER 4: Soft Stretchable Electronics with Wrinkled Microstructures	25
CHAPTER 5: Simple Fabrication Process for Microfluidics	33
CHAPTER 6: Integrating Surface Mounted Technology with Stretchable Circuits	51
CHAPTER 7: Application of Soft, Wearable Sensors for Respiration Monitoring	70
CHAPTER 8: Discussion and Future Prospect	90
REFERENCES	94

LIST OF FIGURES

		Page
Figure 2.1	Cardiovascular System Diagram	6
Figure 2.2	Pulmonary System Diagram	9
Figure 2.3	Pulmonary Function Test Graph	10
Figure 2.4	Skin Diagram	12
Figure 3.1	Fractal Strain Relief Structure	20
Figure 3.2	Strain Relieving Island	23
Figure 4.1	Stretchable Wrinkle Thin Film Sensor Fabrication Process	26
Figure 4.2	Highly Stretchable Wrinkle Gold Thin Film Interconnects	29
Figure 4.3	Highly Stretchable Wrinkle Thin Film Strain Sensor	30
Figure 5.1	Reversible and Irreversible Microfluidic Fabrication Process	37
Figure 5.2	Microfluidic Bond Parameter and Bonding Scheme	38
Figure 5.3	Microfluidic Tissue Chamber Fabrication Process	41
Figure 5.4	Polymer Swell Test	43
Figure 5.5	Bond Burst Pressure Test	44
Figure 5.6	Microfluidic Gradient Generator	45
Figure 5.7	Multilayer Microfluidic Mixer	46
Figure 5.8	Microfluidic Tissue Chamber	47
Figure 6.1	SMD and Stretchable Circuit Fabrication Process	55
Figure 6.2	Different Cove Geometry Design	56
Figure 6.3	Nylon Mesh Island under Strain	60
Figure 6.4	Strain Failure Point for different Cove Geometry	61
Figure 6.5	Circuit Output under Strain	62
Figure 6.6	RC Circuit Output under Strain	63
Figure 6.7	FEA for different Mesh Geometry and Substrate Geometry	64
Figure 6.8	Integrated Strain and PPG Sensor	66
Figure 7.1	Respiration Monitoring Hardware Setup	73
Figure 7.2	Strain Sensor Placement for Respiration Monitoring	74
Figure 7.3	Strain Sensor Adhesion Method onto Human Skin	79
Figure 7.4	Strain Sensor Respiration Calibration Model	80
Figure 7.5	Comparing Measured and Calculated Respiration Volume	82
Figure 7.6	Measuring Respiration Rate and PFT	83
Figure 7.7	Respiration under Motion	85
Figure 7.8	Frequency Decomposition of Respiration under Motion	87

LIST OF TABLES

		Page
Table 5.1	Reversible Microfluidic Burst Pressure after Repeated Use	45
Table 7.1	Respiration Calibration Model Fit	81

ACKNOWLEDGMENTS

I would like to express my sincerest gratitude towards Professor Michelle Khine for always setting new challenges for me and allowing me to grow as a person and researcher in her lab. I have been given opportunities I never would have dreamed up working, so thank you for taking me in and leading me forward. I also want to acknowledge and thank my committee members, Professor Zoran Nenadic, Professor William Tang, and Professor Fadi Kurdahi for taking the time to review my work as a graduate student. Thank you for the input and guidance during my graduate journey at U.C. Irvine.

To my friends and families, thank you for supporting me these past five years. Thank you for taking me out of the lab and reminding me the world is bigger than my workbench. To Diane Choi, thank you for being my constant throughout the past 6 years. I knew that I could always depend on you for love and support any time of the day.

My work here would not have been possible without the countless support of my previous and current labmates and classmates. You are the ones that helped set up my graduate career so I can be here today. To all the undergraduate students that worked with me, I truly appreciate the hard work you put in everyday with my research. Your work has made the result in this dissertation possible. I am grateful for having an environment I look forward to going to everyday.

Lastly, I would like to acknowledge AIP Publishing, Nature Publishing Group, and Royal Society of Chemist for granting me permission for reprinting material in this dissertation.

CURRICULUM VITAE

Michael Chu

EDUCATION

2013 **B.S.** in Bioengineering, *University of California, San Diego*

2016 **M.S.** in Biomedical Engineering, *University of California, Irvine*

2019 **Ph.D.** in Biomedical Engineering, *University of California, Irvine*

POSITIONS

2014 - 2019 **Graduate Student Researcher**, Khine Lab, *University of California, Irvine*

2015 - 2018 **Teaching Assistant**, Biomedical Engineering, *University of California Irvine*

2019 - Now **Co-founder and Senior Researcher**, Makani Science, *Irvine, California*

FIELD OF STUDY

Integrated soft stretchable electronics for respiratory and cardiovascular monitoring

PUBLICATIONS

Chu M., Chou E.F., Zhou Y., Yeung M., Wong K., Cho K., Khine M. Highly Stretchable Circuit with Integrated Surface Mounted Devices for Human Vital Monitoring, *In preparation*

Chu M., Nguyen T., Pandey V., Zhou Y., Pham H.N., Bar-Yoseph R., Radom-Aizik S., Jain R., Cooper D.M., Khine M. Respiration Rate and Volume Measurements using Wearable Strain Sensors, *NPJ Digital Medicine* **2,** (2019)

Chu M., Nguyen T., Lee E.K., Morival J.L., Khine M. Plasma Free Reversible and Irreversible Microfluidic Bonding, *Lab Chip* **17**, (2017)

Kim J., Chou E.F., Le J., Wong S., **Chu M.**, Khine M. Soft Wearable Pressure Sensors for Beat-to-Beat Blood Pressure, *Monitoring, Adv. Healthcare Mater.* **8**, (2019)

Lin L., **Chu M.**, Park S.J., Zakashanky J.A., Khine M. Conformal Stretch Sensors for High Resolution Motion Sensing and Control, *Macromolecular Materials and Engineering* **304**, (2019)

Park S.J., Kim J., **Chu M.**, Khine M. Flexible Piezoresistive Pressure Sensor Using Wrinkled Carbon Nanotube Thin Films for Human Physiological Signals, *Adv. Mater. Tech.* **3***,* (2018)

Pegan J.D., Zhang J., **Chu M.**, Nguyen T., Park S.J., Paul A., Kim J., Khine M. Skin-Mountable Stretch Sensor for Wearable Health Monitoring, *Nanoscale* **8**, (2016)

Park S.J., Kim J., **Chu M.**, Khine M. Highly Flexible Wrinkled Carbon Nanotube Thin Film Strain Sensors to Monitor Human Movement, *Adv. Mater. Tech.* **1**, (2016)

Nokes J.M., Sharma H., Tu R., Kim M.Y., **Chu M.** Siddique A., Khine M., Nanotextured Shrink Wrap Superhydrophobic Surfaces by Argon Plasma Etching, *Materials* **9***,* (2016)

Kim J., Park S.J., Nguyen T., **Chu M.**, Pegan J.D., Khine M. Highly Stretchable Wrinkled Gold Thin Film Wires, *Appl. Phys. Lett.* **108***,* (2016)

Nokes J.M., Liedert R., Kim M.Y., Siddiqui A., **Chu M.**, Lee E.K., Khine M. Reduced Blood Coagulation on Roll-to-Roll, Shrink-Induced Superhydrophobic Plastics, *Adv. Healthcare Mater.* **5***,* (2016)

INTELLECTUAL PROPERTIES

Khine, Michelle; Pegan, Jonathan; Lee, Eugene; **Chu, Michael**; Duhay, Francis. 2018. Predictive Respiratory Monitor and System. US 2018/0129786 A1. Published May 10, 2018

Chu, Michael; Nguyen, Thao; Khine, Michelle; Lee, Eugene. 2016. Self-Adhesive Microfluidic and Sensor Devices. US 2017/0156623 A1. Published Jun. 8, 2017

PRESENTATIONS

Chu M., Kim J., Lin L., Chou E.F., Nguyen T. *Honey, We Shrunk Healthcare! Continuous Physiological Monitoring,* Poster Presentation at CADMIM IAB Meeting, Irvine, CA, (Mar. 2019)

Chu, M. *Conformal Shrink Electronics and other Random Stuff*, Oral Presentation at the Microfluidics, Biosensors and Biosecurity Summit, Coronado Island, CA, (Oct. 2017)

Chu M., Lin L., Nguyen T., Khine M. *Ditch the Lid: Reversible and Open Channel Microfluidics,* Poster Presentation at CADMIM IAB Meeting, Irvine, CA, (Mar. 2017)

HONORS AND AWARDS

2019 Graduate Dean's Dissertation Fellowship, *University of California, Irvine*

2017 Public Impact Fellow, *University of California, Irvine*

2013 James Mead Memorial Award, *University of California, San Diego*

OUTREACH

2015 - 2018 **Curriculum Developer**, 100 Tiny Hands, *University of California, Irvine*

2017 - 2018 **Mentor**, Achievement Institute of Scientific Studies, *Santa Ana, CA*

2012 - 2013 **Cofounder and Vice President**, Teach for San Diego, *University of California, San Diego*

ABSTRACT OF THE DISSERTATION

Integrated Stretchable Electronics for Human Vital Signs Monitoring

By

Michael Chu

Doctor of Philosophy in Biomedical Engineering

University of California, Irvine, 2019

Professor Michelle Khine Irvine, Chair

Continuous health monitoring is of great interest in the medical field because of its potential to improve diagnostics and treatments for patients. Continuous monitoring systems must be comfortable for the patients to wear as well as be able to gather actionable and high-quality data. This usually requires the device to be soft to maintain patient comfort as well as conformal to create a stable interface for high quality signals acquisition. While the last couple of decades has seen an exponential growth in wearable technology and global connectivity, the growth of soft, wearable electronics has been slower. The work presented here focuses on creating a soft, wearable system for monitoring human vital signs. Specifically, simpler fabrication schemes were created for fluidic systems and integrating conventional surface mounted devices (SMD) with stretchable electronics. Finally, a method is presented for measuring vital signs from the respiratory system using highly soft, conformal, and non-obtrusive strain sensors.

Chapter 1: Introduction

The past century has witnessed great strides in medicine. The last decade alone has seen the start of big data integration with machine learning to help make better and more informed healthcare decisions. However, while medical technology has advanced, the overall infrastructure of the healthcare system has remained stagnant. Patients are still expected to travel to a centralized location for discrete, reactionary based care where the healthcare provider only has a brief window to assess the patient's health. Unless the disease symptoms are present at the time of visit, the doctor may not be able to accurately evaluate the patient's health. This could result in delayed or improper diagnosis, which can lead to poor outcomes.[1] Moreover, the decision to see the healthcare provider is ultimately at the discretion of the patient based on their own self-assessment; a wrong decision could lead to further delay in diagnosis or treatment. For example, asthma is a disease that requires constant monitoring and care; if any active symptoms are left untreated, there could be severe consequences, especially in a younger population that may not understand the symptoms of an asthma attack.[2] Other chronic diseases that would benefit from having immediate response to acute symptoms includes congestive heart failure, diabetes, and respiratory diseases like chronic obstructive pulmonary disease.[3–5] This presents a need for remote and continuous vital monitoring that can provide relevant and actionable information for the patients or doctors. The information provided can be used to improve diagnosis or be used in real time to treat exacerbating disease symptoms.

Wireless and remote connectivity has experienced exponential growth at the start of the 21st century. The development of personal smart devices, faster computers, and cloud-based storage has allowed individuals to be constantly connected through the internet. This global

connectivity of devices, termed Internet of Things (IoT), has set the framework for remote monitoring and communication. However, while IoT technology rapidly grew, the technology for remote and continuous human vital monitoring progressed at a slower rate.[6] Some of the most common commercial devices are rigid watch worn monitors that are limited to sensing activity and pulse. More recently, Apple introduced a smart watch with the ability to monitor ECG and detecting abnormal waveforms, and Dexcom released a wearable patch for continuous glucose monitoring.[7] However, current commercial devices can only capture a fraction of the vitals present in the human body and can only provide a limited snapshot into the patient's health. Appropriately, there are great interests in the medical field to develop more tailored sensing systems for monitoring different types of vitals such as blood pressure, biochemicals, and respiration.[8]

When developing wearable vital monitors, there are several considerations that must be addressed. First, the sensors must be discrete and comfortable for the patient. Most wearable devices are in a smaller and softer form factor that allows for better integration with the human body. Secondly, the sensors must have good signal fidelity; the signal acquired should be clean and actionable. For example, there are many commercial devices that can capture respiration rate with high accuracy. Respiration rate by itself provides basic information of a patient's well-being. However, if respiration volume and flowrate are also measured, then the information could potentially help improve diagnostic capabilities. In addition to these basic considerations, there are also more specific requirements specific to soft, wearable sensors that will be discussed later in this dissertation.

The focus of this dissertation will be on the development and application of a soft, wearable electronic platform for monitoring physiological signals from the cardiovascular and pulmonary system. The dissertation is divided into the following parts. Chapter two will report on the types of vitals that can be taken from the body, with specific focus on the biology of the cardiovascular and pulmonary system. Chapter three will examine the requirements for a wearable system; this includes the motivation for using a soft electronic system as well as the current state of the art. Chapter four will discuss the platform for fabricating the soft electronics used in this dissertation. Chapters five and six will explain the development and design of the soft electronic system; this includes a simpler method for fabricating microfluidic systems. Chapter six will focus on a method for integrating traditional passive and active surface mounted components into a soft elastomeric system. This system is used to develop a soft, wearable sensor for measuring pulse. Chapter seven will explore the application of these soft electronics and sensors for measuring respiration rate and volume. Lastly, chapter eight will explore future works and systems that needs to be researched for an improved and wider application of these systems.

Chapter 2: Signals from the Human Body

The human body is a complex network of different systems working together to maintain a healthy individual. Because every system is linked to each other, changes to one area in the body will often result in downstream changes to other systems. For example, when a person performs physical activity, the metabolic demand increases, which requires more oxygen for the muscles. To meet the oxygen demand and to remove carbon dioxide from the system, the body increases the respiration rate, volume, and heart rate. A new equilibrium is formed until the body's increased demand for oxygen stops. This type of response to physical activity is understood to be normal, thus any deviation from this response may indicate a potential problem. Generally, proper understanding of the normal and abnormal state of the human body, and identifying the abnormal state, is the first step in diagnosing and treating the patient. This requires a good understanding of the signal type, signal quality, and normal signal that can be measured from a system. Chapter two will start by exploring the different signals that can be measured from the body with an emphasis on the cardiovascular and pulmonary system. Afterwards, the dynamics of the skin will be examined to understand how the skin will affect signal quality of wearable monitoring systems.

2.1: Signals from the Human Body

The overall type of signals that can measured from the body can be roughly divided into four categories.[9] The first category is the measurement of mechanical deformation or movement generated by the body. For example, respiration uses a series of muscles to expand the lung; this action also stretches the skin covering the torso. We demonstrate, in this dissertation, that it is possible to calculate respiration rate and volume using the strain from the torso due to respiration. The next category of signals that can be measured are electrical signals generated by the body. These types of signals can be naturally created by the ion gradients that forms in muscles and nerves. A sudden change in the gradient is normally associated with some form of actuation or event and can be measured. A signal can also actively be injected into the body to measure different properties such as impedance. The third category is optical measurement, which examines the way an injected light interacts with the body. Unless done invasively, this process is typically superficial, with light penetrating roughly 5 mm into the body.[10] Techniques like photoplethysmography, injects a light of a certain wavelength into the body and measures the light reflected back using a photodiode. If the LED colors are changed to Red and Infrared wavelengths, which is absorbed differently by oxygenated and deoxygenated hemoglobin, then blood oxygen saturation can be measured as well. The last category is non-invasively measuring chemical signals from the body, such as glucose, ions, or proteins. This method almost entirely focuses on liquid samples such as sweat, urine, and tears. Sweat has garnered much interest because of its easy, continuous access compared with urine or tears. There has been many different systems developed for point of care monitoring on the skin.[11]

2.2: Cardiovascular and Pulmonary System

2.2.1: Overview of the Cardiovascular System

The cardiovascular system is the lifeline of the body. It supplies the body with oxygen, stored by hemoglobin in the red blood cell, and nutrition while cycling the waste to be removed. [12] The driving force of this system is the heart, which pumps blood through the lungs and body in discrete beats. Deoxygenated blood starts by being pumped through the lungs by the right heart to be oxygenated and for carbon dioxide to be removed. Afterwards, the oxygenated blood

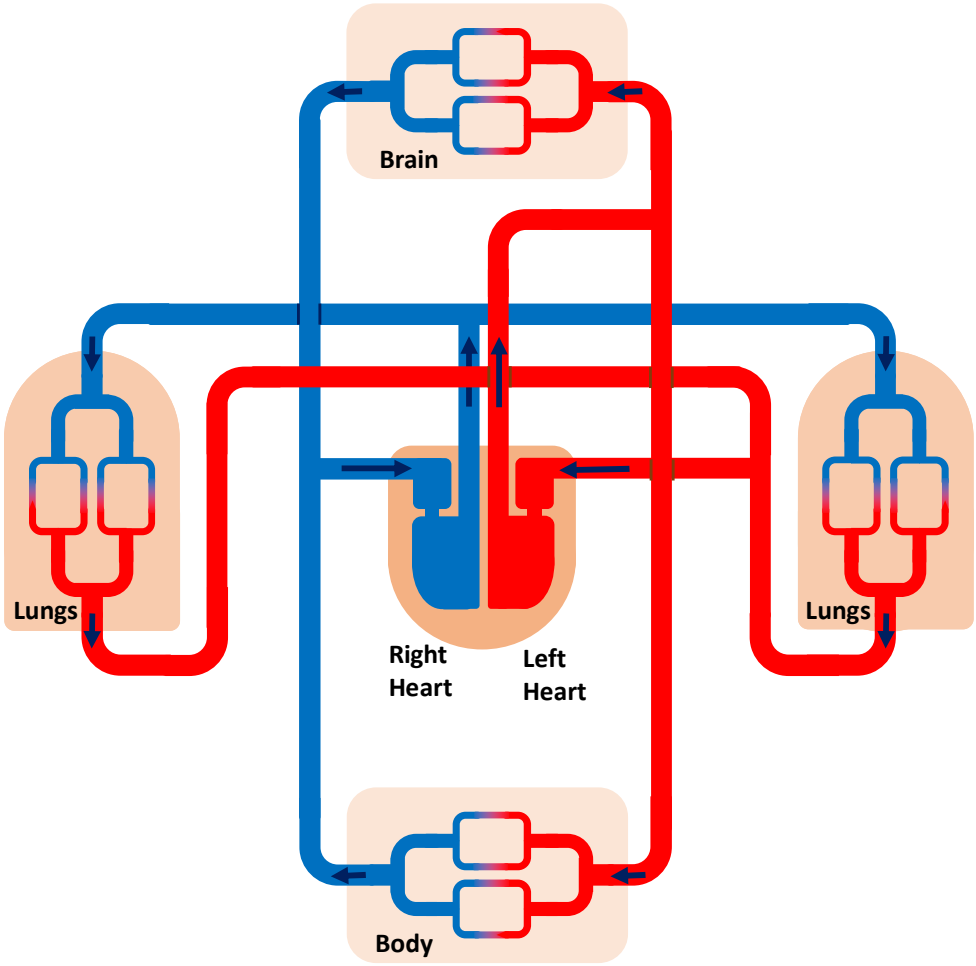

Figure 2.1. Diagram of the blood flow through the cardiovascular system.

is then returned to the heart to be pumped through the rest of the body (Figure 2.1). Each beat of the heart produces an increase in blood pressure and volume that travels through the blood vessel. As the blood passes through the branching blood vessel from the arteries to the capillaries, it'll experience an increased resistance. Eventually the pulsatile waveform will be attenuated as the blood flows back to the heart through the venous system.

There are different types of signals that can be noninvasively extracted from the cardiovascular system at different points in the cardiac cycle. At the start of the heart contraction, the biopotential generated during beating of the heart can be measured using an electrocardiogram (ECG). After the contraction, the resulting pulsatile waveform through the blood vessels can be measured either mechanically or optically. Optical methods are commonly and commercially used to measure pulse rate. Peripheral blood oxygen saturation (SpO_2) can also be calculated by using different wavelength of light to extract the ratio of oxygenated to deoxygenated hemoglobin in the blood. Mechanical measurement of the system, by measuring the distention of the arteries through each beat, could be taken extract information on blood pressure and vasculature health.

The health of a person can be assessed different cardiovascular signals measured. The shape of the ECG, through different placement on the body, can be used to identify different diseases such as heart attacks and arrhythmias. The peak to peak interval from either the ECG or pulse waveform can be used to calculate heart rate variability (HRV), which shows the heart's reactivity to different activities; higher HRV is an indication of a healthier heart. There are studies to show that the HRV measured through optical methods on smart watches can also be used to identify atrial arrhythmias.[13] General vascular and blood pressure can be determined using the

pulsatile waveform. If both the ECG and pulse measurements are combined, then Pulse transit time (PTT) can be measured by calculating the inherent lag time between the ECG and the pulse. This can be used to determine general health on the vasculature system as well as calculate blood pressure. These measures by themselves, can provide important information on a patient's health; however, when combined with other signals such as respiration, it can provide a more comprehensive picture of the patient's health.

2.2.2: Overview of the Pulmonary System

If the cardiovascular system is the most important system of the body, then the pulmonary system comes as a close second. These two systems are directly linked to each other, and one cannot operate without the other. While the job of the cardiovascular system is to move nutrition, oxygen, and waste through the body, the pulmonary system's job is to provide oxygen and remove carbon dioxide from the blood through gas exchange.

The pulmonary system is composed of the airways, lungs, and muscles required for actuating breathing.[14] There are two primary mechanism for breathing in healthy individual (Figure 2.2). The first, and main, mechanism is through the diaphragm. The diaphragm is a muscle that sits right below the lungs. When the muscle contracts, it pulls the pleural cavity which contains the lungs. This creates a negative pressure in the intrapleural space, which pulls the lungs down. A negative pressure is then created in the lungs, with respect to atmospheric pressure, causing air to enter the lungs. As the diaphragm contracts, it pushes the organs in the abdomen down and out, extending the stomach region of the body. During exhalation, the diaphragm relaxes, and the elastic nature of the tissues compresses the lungs. The second main mechanism used for breathing is through expansion of the chest wall using the interstitial muscle

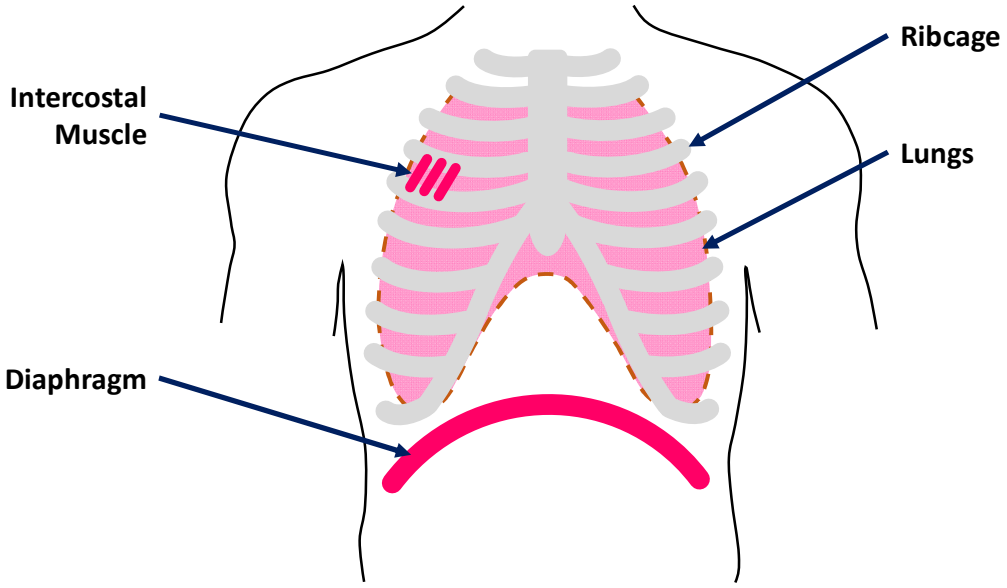

Figure 2.2. Diagram of the lungs, ribcage, and diaphragm. The intercostal muscle moves the ribcage and chest wall during respiration to change the volume of the lungs. The diaphragm pulls on the pleural cavity during respiration to increase the lung volume.

between the ribcage. As the muscles contract, the ribcage expands, again pulling the pleural cavity and creating a negative pressure to expand the lungs and the chest wall. Similarly, exhalation occurs when the muscles relaxes, and the natural elasticity of the tissue between the ribcages compresses the lungs. Additionally, there are muscles within the interior of the ribcage that contract to further compress the lungs and force air out.

Like the cardiovascular system, respiration is a periodic signal that can be characterized by the signal's amplitude and frequency. The amplitude for respiration is the volume of air exchanged per breath; this is also called respiration volume. The frequency is the breath rate, or the number of breaths taken per minute. The respiration velocity, or flowrate of each breath, is

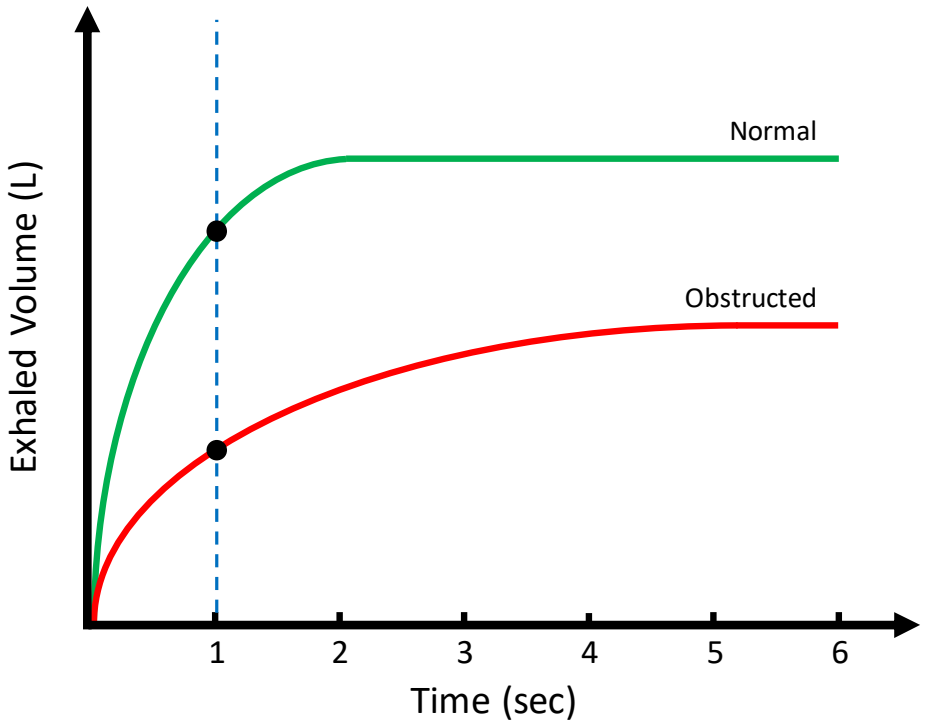

Figure 2.3. Spirometry based pulmonary function test (PFT). The green line represents a normal PFT while the redline represents a PFT with an obstruction. The vertical line is the volume exhaled during the first second for the FEV1.

another important parameter that is measured as well. Other parameters that are often examined includes the composition of oxygen and carbon dioxide in each breath to determine metabolic activity, as well as listening for the sound of the air moving through the airway to determine any restriction or obstruction of breathing.

There are different ways for determining respiratory health in a clinical setting. At a minimum, medical professionals typically look at the respiration rate and listen for any obstruction in the respiratory tract. In a general hospital setting, respiration rate is one of the main parameters that is looked at to determine patient health. Any prolonged values outside of the normal range, 12 to 20 breaths per minute, would require immediate response. Being able to measure the depth of the respiration is important as well, although not as common. A patient

may be breathing with a normal rate but at a much more depressed breathing, which would decrease the amount of oxygen exchanged. Normal respiration depth should be about .5 L per breath. Respiration volume and rate are also be combined to form a parameter called minute ventilation, which describes the total amount of air a patient is exchanging per minute.

If a deeper analysis is required, then a series of respiratory tests, called pulmonary function tests (PFTs), could be performed. PFTs are noninvasive tests where the subject breathes under certain conditions and maneuvers to assess lung function. Spirometry is a common type of PFT where the subject inhales deeply and completely and forcefully exhales until there is no air left in their lungs. The total volume of the air exhaled is measured over time (Figure 1.3). The volume of air exhaled can be examined at different points. Commonly, physicians will calculate the forced expiratory volume at 1 second (FEV1) and take it as a ratio over the total expired volume, also called the forced vital capacity (FVC). The ratio of FEV1/FVC, also called FEV1% will inform of any resistance of obstruction in the airway. A lower ratio will indicate that the patient cannot quickly expel air, normally due to increased resistance in the airway. Any value below 70% is abnormal.

2.3: Wearable Sensors and the Human Skin

The human skin is the body's first line of defense against the external environment. The epidermis passively keeps contaminants and germs out while helping to maintain an equilibrium within the body. Accordingly, the skin is a very effective barrier, not only to the external world, but also for keeping signals within the body.[9] In order to create an effective wearable monitoring system, the properties of the skin must be accounted for.

2.3.1: Properties of the Skin

The skin is a composite consisting of three distinct layers with each layer having additional sublayers (Figure 2.4). The outermost layer, called the epidermis, serves as the primary barrier between the external environment and the body. The epidermis is composed of layers of dead and live cells with a total thickness between 75 to 100 µm. The second layer, also known as the dermis, is a consist of fibrous tissue and vascularization; this layer is approximately 1.5 to 2.5 mm

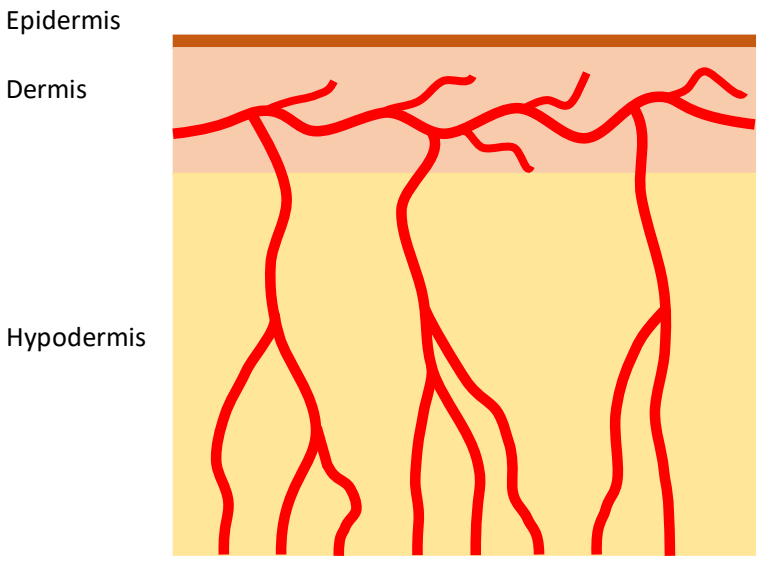

Figure 2.4. The different layers of the skin. The epidermis the most exterior layer that is not vascularized. The dermis and hypodermis are thicker, vascularized layers.

thick. The last layer, the hypodermis, is made of subcutaneous fat. This layer tends to be thicker than the epidermis and dermis; moreover, the thickness of the hypodermis is dependent on its location around the body[15]. Because most wearable sensors interact with the epidermis and dermis, the following sections will focus on those two layers. However, the hypodermis should not be completely discounted because the layer of fatty tissues may attenuate or change the signal of interest. This layer should be accounted for accordingly for certain devices.

The epidermis can be divided into two layers. The outermost layer is composed of dead cells with very low moisture while the inner layer is made from live cells that contains the pigmentation for the skin. This layer of pigmentation is the first barrier that any optical signal must past through to reach the dermis. Because the exposed epidermis is so dry, it has incredibly high impedance, which significantly attenuates any electrical measurements through the skin. Unfortunately, most natural occurring biopotential has very small voltage small. The combination of high impedance, and small signal, makes biopotential signals difficult to measure using dry electrodes and very susceptible to noise. Any signals measured using dry electrodes should be amplified immediately before the signal is loss.

The dermis is a very complex layer that is composed of connective tissues, fibrous proteins, and blood vessels. The Young's modulus ranges from 2 to 80 KPa[16]. This layer contains the elements that are responsible for the non-linear mechanical behavior of the skin, which should be considered when applying mechanical sensors. At smaller tensile strains, the elastin in the dermis is responsible for the linear mechanical behavior of the skin. However, as the strain increases, the behavior becomes more non-linear, until irreversible changes occur at about 30%

strain[15–17]. This means most wearable sensors would need to operate up to 30% strain without failure.

2.3.2: Other Considerations for the human skin

The human skin is also a dynamic environment that changes over short and long periods of times. In the short term, the skin actively produces oil and sweat which may change the softness and dryness of the external environment. The skin can also react acutely, and generally negatively, to different materials such as nickel, latex, etc. Over longer periods of time, the mechanical properties of the skin will start to change as well. As people start to age, the skin will lose elasticity and become softer and more wrinkled. Conversely, at a younger age, the skin is very thin and sensitive to the environment. All these factors combined will affect the consideration for the construction of wearable device as well as direct the adhesive and material choice of the sensors.

2.4: Conclusion

Understanding the type of signal that can be acquired from the body is important when designing wearable vital monitors. Highly quality physiologically relevant signals can be extracted if there is a good understanding of the biology for the signal of interest. For example, respiration volume is a value that is normally calculated based on airflow in or out of the lungs. However, knowing that the torso will distend proportionally to the respiration volume allowed researchers to calculate respiration volume from strain of the chest and abdomen, seemingly unrelated signals.[18] A comprehensive understanding of the signal type and pathway can help build sensors that can extract high quality physiological signals while minimizing artifacts.

Another important consideration for creating non-invasive wearable monitors is the human skin. The majority of health monitors will interact with the skin and having a good understanding of the skin's property can help developed higher quality sensors. The skin has a Young's modulus between 2 to 80 kPa and a maximum strain of 30%. Thus, wearable soft sensors should have a similar modulus and be able to operate repeatedly up to 30% strain without failure.

Chapter 3: Soft Electronics Requirements and Background

Soft stretchable electronics (SSE) can operate in environments traditional printed circuit boards (PCB) cannot. For example, the human body is very soft and dynamic environment that the typical hard PCB cannot attach to. The inherent stiffness mismatch between the two material, the skin and the PCB, creates areas of high stress concentration that causes delamination between the two material. A poor interface between the sensor and the skin makes it very difficult to measure signals from the body. A better interface could be created by applying additional forces, pressure, and adhesives between the electronics and the skin; however, that creates an environment that is highly uncomfortable for the patient. Thus, there are certain requirements need to be satisfied in order to create electronics that can maintain a good interface while being comfortable for the patient. Chapter 3 will start by reviewing these requirements for soft, wearable system. Afterwards, a high-level overview of flexible electronics will be described.

Chapter 3.1: Requirements for Soft Electronics as a Wearable System

There are many different types of considerations that should be accounted for when designing wearable monitors. From the patient side, it is important to ensure patient safety as well as patient comfort. From the hardware side, it is important to have a monitoring system that is not only robust on the human body but can also be integrated with the current wireless infrastructure. At the interface between the electronics and the skin, it is crucial that highly quality and actionable signals can be acquired. Lacking in any one of these categories will result in an incomplete system.

Implicitly, any type of monitoring system cannot cause harm to the patient. Thus, biocompatibility of the device is incredibly important. Use of material that tends to be inert, such as noble metals, will be more beneficial better than using material with known common allergies, such as nickel and latex. While there are many novel conductive materials that can be used for fabricating electronics, such as carbon nanotube, there is still very little data on the compatibility of the material with the body. Patient comfort is another important criterion for wearable devices. Because the patient is required to wear the system for longer periods of time, patient comfort is important for patient compliance. Having a soft stretchable system, with a modulus like the skin, will be more comfortable than a stiff backing. Moreover, having a device that is small, lightweight, and low profile, will allow the device to be discrete and nearly unnoticeable.

High fidelity and actionable signals are incredibly important for any diagnosis or monitoring system. Good signal quality requires unimpeded transfer of or transduction of energy between the body and the sensor. This typically requires a stable interface between the two system that will not interfere with the signal. Soft, wearable sensors that is intimately laminated

and moves with the skin generally provides a better interface. Thus, having a soft stretchable material with a stiffness similar to the skin reduces the chance of delamination and also moves with the skin. Having a proper adhesive is also important in creating a stable interface. The adhesive used should be biocompatible and also be adjusted for the age and sensitivity of the skin.

For a wearable system to be truly functional, it should be able to operate remotely and wirelessly. Typical systems have some sort of short-range communication method that pushes data to a smart device, which then uploads the data to the cloud. Examples of this includes using near field communication (NFC), Wi-Fi, and Bluetooth. However, before the data is sent to the smart device, the signal is typically processed and amplified through an analog circuit. This involves using passive and active circuit components as well as integrated circuit (IC) components. While there has been research done to develop flexible circuit components, the work is still immature, and a commercially available fully stretchable electronic systems are still not available. In order to create a wearable system that is compatible with the current electronic infrastructure, conventional hard circuit component must be integrated with soft stretchable electronics. This generally involves combining surface mount devices (SMD) with soft stretchable wires and sensors.

3.2: Soft Electronics: Current Standard, Research, and Limitations

Soft stretchable electronics are generally created by choosing soft and stretchable conductors or introducing strain relieving geometries to make an otherwise stiff and brittle material stretchable. Whatever process used, the end goal is to create a softer, stretchable, conformal system that is robust enough to operate in a dynamic environment such as the skin.

3.2.1: Material for Stretchable and Flexible Conductors

There are many methods in literature for creating stretchable electronics. In almost all cases, the typical fabrication method involves setting the function material into a soft elastomeric substrate. These schemes vary in the type of conductive material used to create the stretchable conductor.

Conductive polymer generally leverages a conductive filler or particle, such as silver particles or carbon nanotube suspended in an elastomer, creating percolating networks of conductive particles that form electrical pathways[19,20]. The number of particles required to create this electrical pathway is called the percolating threshold and varies between materials[21]. An alternative way of suspending a conductive network within a polymer is by creating a percolating film of the conductive particles or wires before embedding it into an elastomer[22]. Another method is to just make the polymer itself conductive. This is commonly done with the polymers like poly(3,4-ethylenedioxythiophene) or a complex with poly(styrene sulfonate).[23,24] The conductive polymer has the benefit of having highly stretchable wire with a modulus closer to that of the substrate. However, they tend to have higher resistance and may also require high ratio of filler to polymer to achieve the percolating threshold.

Using liquid metal as a conductor is another way to form stretchable wires. Researchers commonly use metals such as Gallium Indium embedded into channels in the elastomer to form the stretchable wires[25–27]. This has the advantage of having super high conductivity with no stress point in the wire to serve as a failure point. However, this fabrication process is difficult making it an impractical method for scaling. Moreover, there are limited methods reported in literature that demonstrates connection with typical electronics.

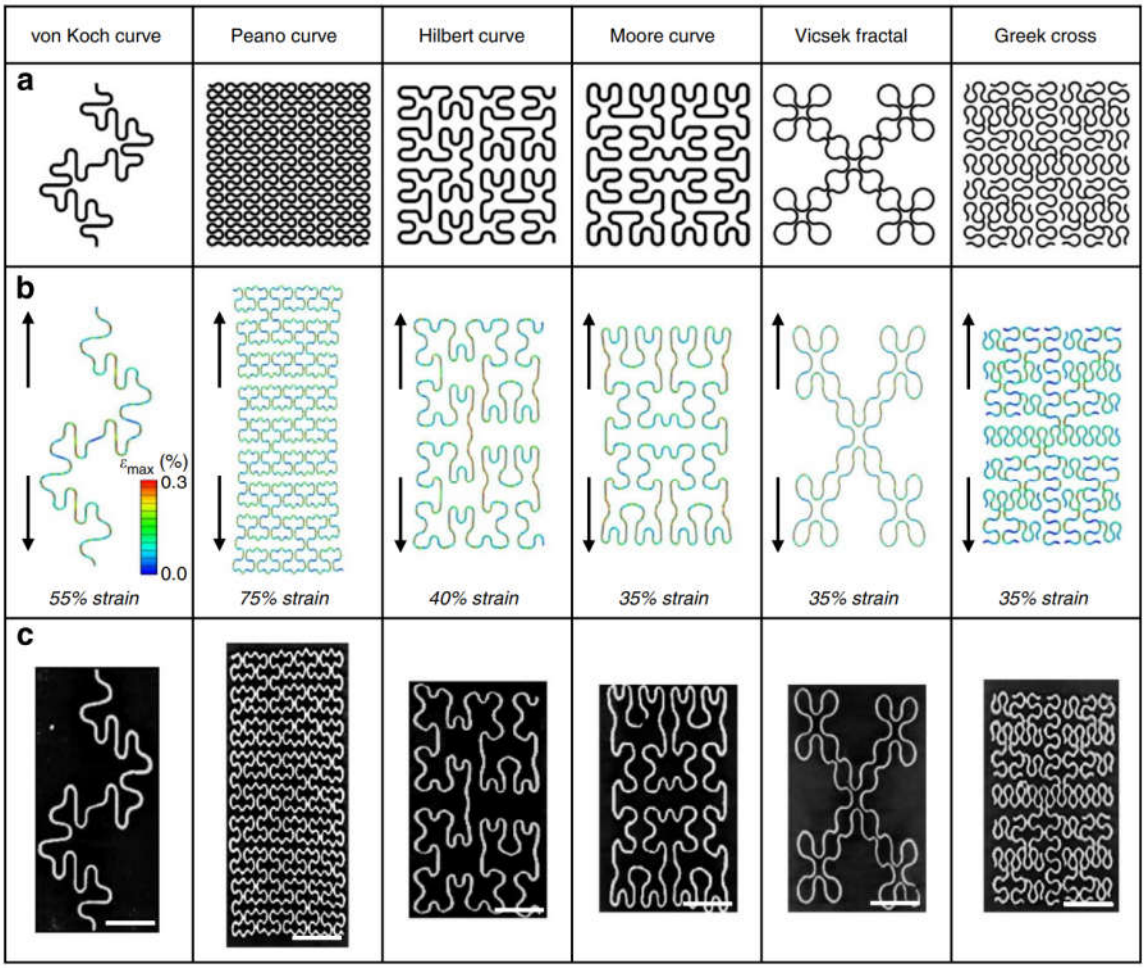

Figure 3.1. Fractal geometries used for creating stretchable thin film wires.[29] This work is licensed under a Creative Commons Attribution 4.0 International License.

Surprisingly, conductive thin films can also be used to create stretchable electronics. Typically metal thin film bonded to an elastomeric substrate can only strain up to ~1%.[28] However, the failure point of the thin film can be increased by incorporating different in plane and out of plane geometrical designs and structures. Researchers built fractal patterns into conductive gold thin films to help delay large stress concentrations (Figure 3.1).[29] Incorporating the fractal pattern with metal thin film that has a thickness of hundreds of nanometers creates system that is highly conformal when applied directly to the skin.[16,30] Other conductive thin film based wires incorporates out of plane sinusoidal wave like structures to help the thin film strain further. These systems are normally fabricated by pre-straining the elastomer substrate a set distance before depositing a metal thin film.[31–33] Afterwards, the elastomer is allowed to relax, forming the wrinkled structures in the film. These systems are most similar to traditional PCB compared to the liquid metal and conductive polymer scheme. Moreover, they have been demonstrated to be able to be integrated with SMD. However, these conductors are limited by their fabrication process. Fabrication of the fractal-based metal thin film is tedious and normally involves transferring a supported free-standing thin film into an elastomer substrate. The thin film with the incorporated wrinkled wave structures can only strain out to the amount it was pre-strained.

3.2.2: Strain Relieving Strategies and Integration with Surface Mounted Devices (SMD)

One of the most common failure modalities for soft electronic is the formation of a catastrophic fracture in the circuit. These points of failure tend to occur in areas with high stress concentration during mechanical deformation. For example, any hard/soft interfaces in a soft electronic system will have high stress under strain.[34] The conductive wires at these locations will

often fracture first, causing premature failure.[35] This is especially a concern when integrating SMD onto stretchable or flexible circuit boards, where there is a large stiffness mismatch between the SMD and the substrate. Accordingly, researchers have developed different methods to remove areas of high stress concentration to minimize premature failure of the circuit.

The stiffness mismatch between the SMD and the substrate could be mitigated by using a substrate with a stiffness similar to the components. Researchers have fabricated stretchable metal wires with serpentine strain relief geometry where devices SMD could be directly soldered on. When stretched the strain relief geometry of the wire will deform before actual interface before the SMD will; this allows the circuit to be stretched without failure at the interface between the SMD and the wire.[36,37]

Lu *et al.* has created a method for integrating SMC with liquid metal wires.[38] Their approach uses a custom fabricated polymer with an anisotropic dispersion of conductive Gallium in the vertical direction of the polymer. This polymer layer is then laminated over pre-formed Gallium wires and the SMD are placed on the polymer over the wires and compressed until the anisotropic dispersion of Gallium Indium forms a connection between the wires and the SMD. While their method does not inherently control the stress concentration around the device, the Gallium itself is highly elastic allowing the device to stretch to 60% strain.

Another method used to limit the stress concentration around SMD, and interconnect interface is to completely isolate the interface from strain. This is can be done by placing strain isolating islands, normally hard, non-deforming materials, under the location of the SMD and wire junction. Alternative methods also include selective stiffening the polymer under the SMD or building the SMD on stiffer polymers.[39] These islands will essentially protect the SMD from any

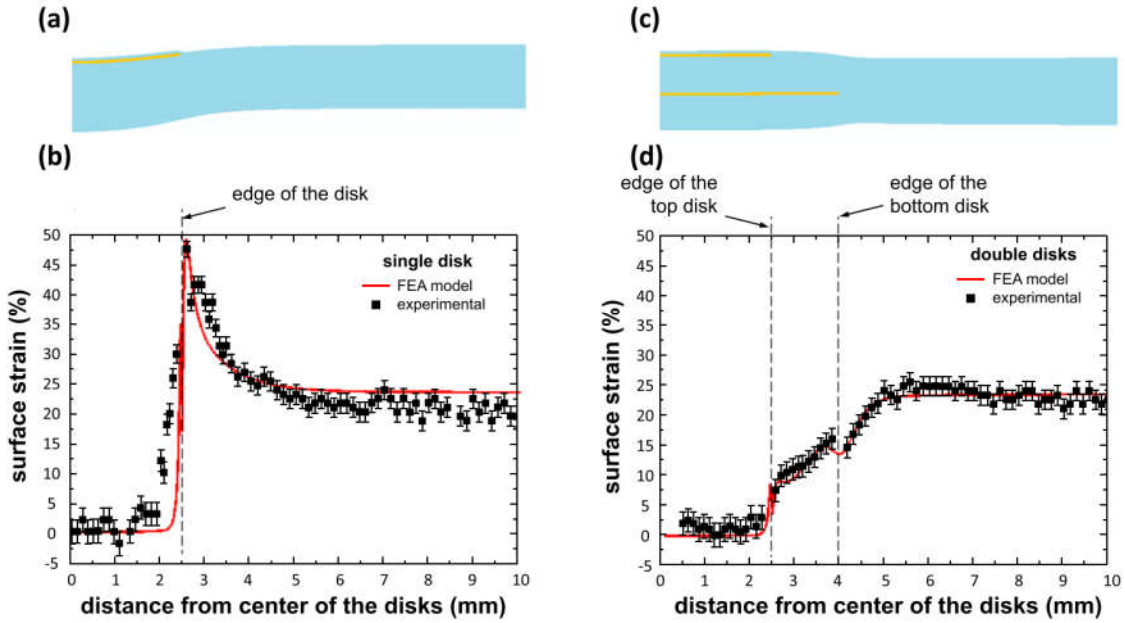

Figure 3.2. Demonstration that placement of two stiff plates placed concentrically over each other will reduce the strain concentration at the edge of the first disk.[28] Reprinted with permission.

stress or movements; however, the stress concentration will instead form at the interface between the island and the substrate.[40] The distribution of stress can be controlled around the strain relieving islands; Robinson *et al.* demonstrated that by incorporating two rigid island under the SMD, a more graduate strain gradient could be formed instead of one with a high strain boundary (figure 3.2).[28]

3.3: Conclusion

Overall, any non-invasive soft, wearable system should be optimized to operate on the dynamic environment of the skin. This generally requires having a system with a modulus similar to the skin that can withstand a minimum of 30% strain. Moreover, because the system will be directly interacting with the patient, it must also be biocompatible with adhesive, formulated specifically to the type of skin of the patient population. For the wearable monitor to be compatible with modern wireless infrastructure, it is also important to be able to integrate the system with conventional surface mounted technology. It is important to ensure that there is minimal failure at the interface between the SMD and the soft stretchable electronics.

Chapter 4: Soft Stretchable Electronics with Wrinkle Microstructures

A variety of methods for fabricating soft stretchable electronics (SSE) was described in the previous chapter. While they all have their unique advantages, they tend to have difficult fabrication scheme or are not commercially viable. The method used in this dissertation is a low cost process that has had preliminary integration with commercially available roll to roll fabrication processes.[41] In this method, highly stretchable and flexible metal thin film electronics are fabricated using commercially available shrink film. The electronic designs are first patterned onto the film and then shrunk. In the shrinking process, nano- and micro- scaled wrinkles are formed in the metal thin film; the wrinkled metal thin film is then transferred into a soft elastomeric substrate (Ecoflex 00-30), which has a young's modulus similar to the skin. The nano- and micro- wrinkle structures in the thin film significantly improves the robustness of the film, allowing to stretch to significant strain without failure. The following chapter explores the fabrication process and parameters in creating the soft stretchable electronics used in this dissertation.

4.1: Fabrication of the Wrinkle Microstructures

The process for forming the wrinkle structures was first developed by Kim and Pegan *et al.*[42,43] Figure 4.1 shows the process flow for the fabrication of a stretchable strain sensor.[44] First, the pre-stressed thermoplastic is masked with a shadow mask in the shape of the sensor or design of interest. The pre-stressed thermoplastic used in this case is pre-stressed polystyrene (PS). The masked PS is then placed into a sputter deposition machine (Quorum magnetron) and the metal of interest is deposited. For flexible gold wire, 40 nm of gold is deposited; for stretchable strain sensors, 5 nm of platinum and 5 nm of gold is respectively deposited. Afterwards, the shadow mask is removed, and the metal deposited PS is placed into an oven preheated at 140^{o} Celsius. After the PS passes its glass transition temperature, the polymer will

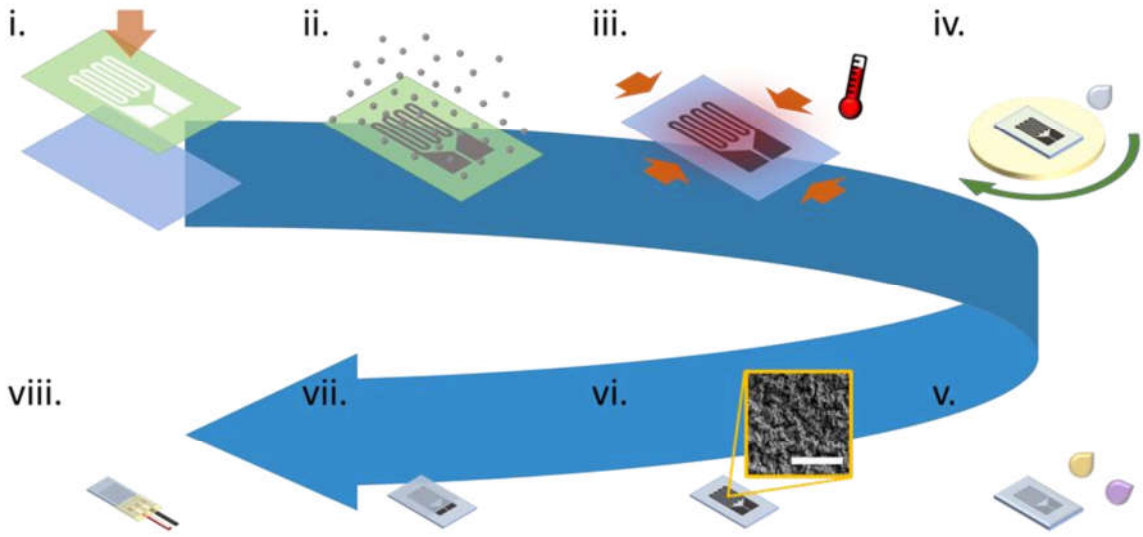

Figure 4.1. The fabrication process for the stretchable wrinkled metal thin film. (i) A shadow mask is first placed over the polystyrene. (ii) The metal of interest is deposited over the mask. (iii) The shadow mask is removed, and the polystyrene is placed in the oven to shrink. (iv) A layer of elastomer is deposited over the shrunk device. (v) After the polymer cured, the polystyrene is removed using acetone and toluene. (vi) The surface of the metal thin film has integrated micron sized wrinkle structure. (vii) The device is encapsulated. (vIII) Wires are attached onto the device.[44]

shrink back to its original shape, compressing the metal. Due to the stiffness mismatch between the metal thin film and the PS, the metal thin film will buck under the compressive stress. The shrunk sensor is then treated in a 5mM solution of 3-mercaptopropyl trimethoxysilane (MPTMS) for 1 hour. Afterwards the sensor is washed with ethanol and a layer of uncured silicone elastomer is then placed over it. The MPTMS will act as a molecular glue between the silicone and the gold, effectively bonding the silicone and gold together. After the silicone elastomer has cured, the PS is then removed in an organic solvent bath. The sensor is first placed in acetone to allow the PS to soften and for the metal and elastomer to fall off. Afterwards, the sensor is cleaned more thoroughly in Toluene. The sensor is then encapsulated in another layer of silicone to protect the metal surface.

4.2: Properties of the Wrinkled Microstructures

The wrinkle structures play a key role in increasing the dynamic range and robustness of the metal thin film. First, the wrinkle structures will deform under strain preventing any premature concentration of stress and delaying crack formation. After a certain strain percentage, cracks in the metal thin film will inevitably form. We believe that the wrinkled structures in the thin film will also help control the crack propagation in the film. The cracks will naturally form at the valleys of the wrinkle, and they will continue to propagate until they reach the end of the valleys. This ultimately helps prevent any catastrophic cracks from forming early.

The effect of the flexible electronics also depends on the type of material that is deposited on the shrink film. We previously demonstrated that wrinkled gold thin films can be strained significantly without a large change in resistance.[42] If that material was changed to a more brittle metal such as platinum, then there is a more significant change in resistance for a given strain, and the resulting thin film can be used as a strain sensor.[43] If the material was changed to carbon nanotube, then an even larger strain can be achieved with different regimes of sensitivity, starting for extremely insensitive to very sensitive.[45]

4.3: Highly Flexible and Stretchable Soft Electronics

As previously mentioned, these wrinkle metal thin films have been used to fabricate highly flexible wires as well as sensors. This dissertation further explores the application of the flexible system in terms of its integration with SMD, as well as using the wrinkle-based strain sensors to measure respiration.

4.3.1: Stretchable Gold Wires

Kim *et al.* created inherently stretchable interconnects by embedding a wrinkled gold thin film in a silicone-based elastomer (Ecoflex 00-30).[42] His work demonstrated interconnects that was able to stretch up to 100% strain without a significant change in resistance (figure 4.2). The film itself was able to stretch past 200% until failure. They also showed that there was minimal cracking in the film at 70% strain, demonstrating the strain relieving features of the wrinkles. At 150% strain, there was clear fracturing that occurred; accordingly, this was also the regime where there was rapid growth in resistance per strain.

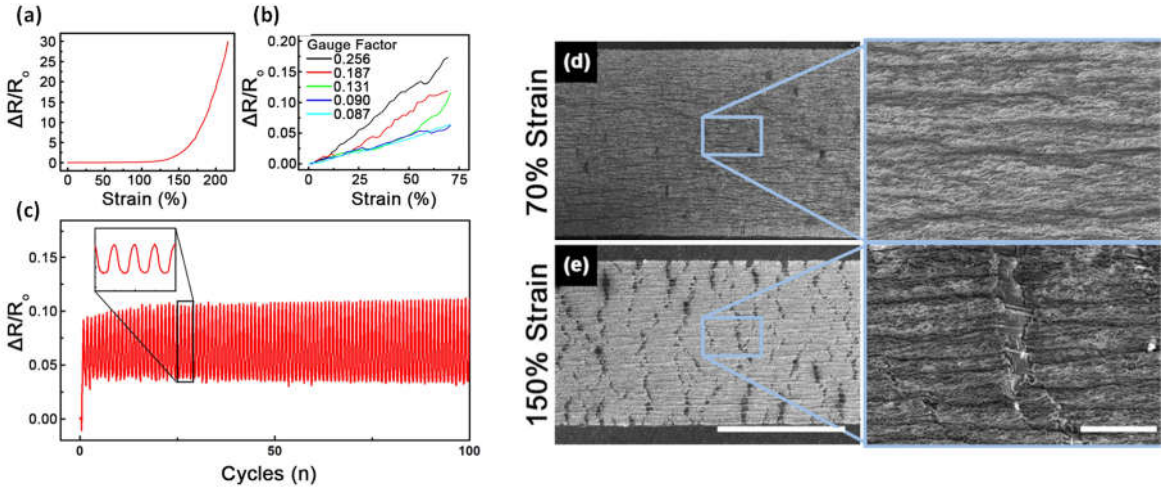

Figure 4.2. (a) A representative graph of a gold interconnect strained to failure. (b) Graphs of the gauge factors across all interconnect. (c) Cycling data of the interconnect up to 100 cycles. (d-e) Scanning electron microscope images of the wrinkled thin film under strain.[42]

4.3.2: Stretchable Strain Sensors

Highly stretchable piezo-resistive strain sensors were created by Pegan *et al.* by changing the thin film material to platinum and gold.[43] Sensitivity for strain sensors is defined by the gauge factor (GF) which is defined as:

$$GF = \frac{\Delta R/R_o}{\Delta L/L_o}$$

where R_o and L_o are the initial resistance and length and ΔR and ΔL are the change in resistance and change in length respectively. This is a measure of the relative change in resistance for a

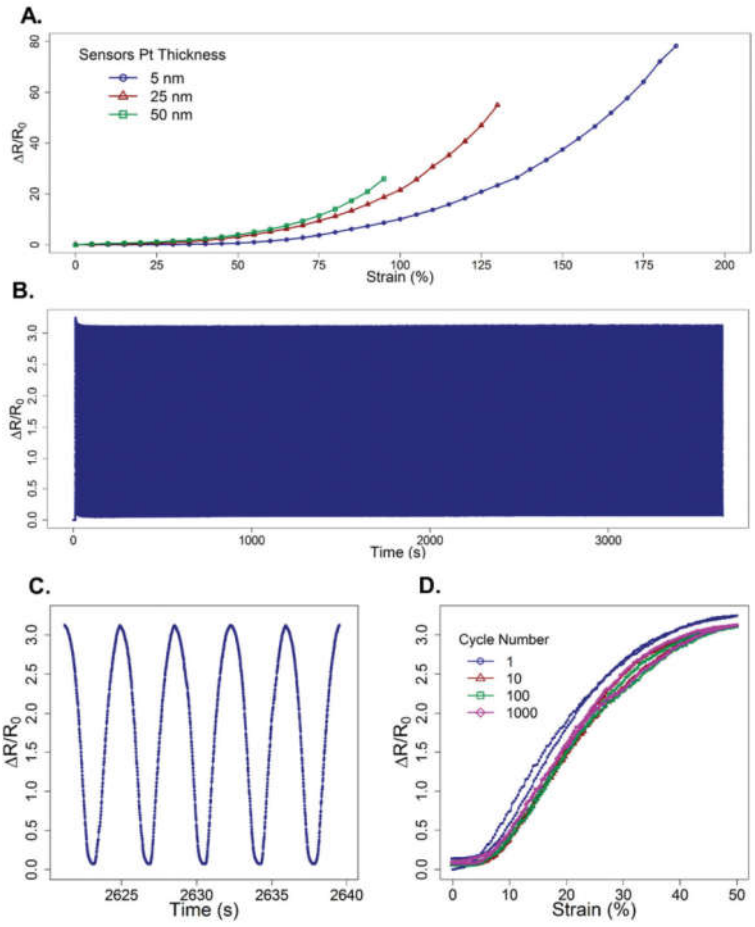

Figure 4.3. (A) Sensitivity curve for strain sensors with varying thickness of platinum. (B-C) Cycling data for the strain sensors. (D) Plot of the normalized change in resistance for the 1, 10, 100, and 1000th cycle.[43]

given strain. Generally, stretchable strain sensors have a tradeoff between sensitivity and dynamic range. Sensors with high dynamic range normally has low sensitivity (GF<1) while sensors with low dynamic range has a high sensitivity. Pegan *et al.* was able to create a stretchable sensor with both a high sensitivity (GF=42) and a large dynamic range (strain=185%); moreover, the sensitivity of the system is tunable by varying the thickness of the platinum layer (figure 4.3). The sensor was also able to go through 1000 cycles of tensile strain with relatively high stability. Using this sensor, he demonstrated initial proof of concept for measuring respiration on the torso. This concept was explored much more in depth in this dissertation.

4.4: Conclusion

The stretchable metal thin film used in this dissertation is a low-cost process that creates inherently stretchable metal thin film traces. The process relies on fabricating the devices on commercially available shrink film to create nano- and micro- sized wrinkles after shrinking the film. After transferring the wrinkled metal thin film into a soft elastomer, the entire device can be stretched without early failure of the film. We believe that the wrinkle geometries in the film helps to relieve any stress concentration by deforming and also controls fracturing of the thin film at higher strains. Deposition of different material can create stretchable thin films with different gauge factors. If only gold is used, then there is very minimal change in resistance during strain, making the thin film ideal interconnects. If platinum is deposited as well, then the thin film becomes a highly sensitive strain sensor.

The work described in this dissertation uses both the interconnect and strain sensor to create a wearable vital monitor. The highly stretchable gold interconnect was integrated with conventional surface mounted components to create stretchable circuits. The soft strain sensors were applied for measuring respiration rate and volume. The two systems were also married together to form a system that can measure respiration and pulse.

Chapter 5: Simple Fabrication Process for Microfluidics

5.1: Introduction and Motivation

One of the ultimate goals of ubiquitous physiological monitoring is to monitor both physical and chemical signals. Some of the most common chemical signals that are measured from the body are analytes from sweat. One method that has been demonstrated for sweat analysis is to implement a wearable microfluidic system on the skin.[46] This type of system would only require a small amount of sweat, making collection and analysis faster and more possible. For example, Koh et al. created a wearable colorimetric based microfluidic patch that collects and analyzes sweat remotely.[46] Their system relies on traditional microfluidic fabrication technique to form a stretchable and wearable, multilayer microfluidic system. However, most traditional Microfluidic fabrication schemes are not scalable, making it difficult to have a widespread application of this system.

Most microfluidic devices are constructed from polydimethylsiloxane (PDMS). This is a stretchable and flexible silicone-based elastomer. While silicone-based elastomers do not easily bond to other materials, a covalent bond could be formed between PDMS and other silicone-based substrates, such as glass or PDMS, by oxygen plasma treating both surfaces and placing them in contact with each other. This is the ubiquitous method for forming PDMS based microfluidic devices. However, while this method produces a very strong seal, there are multiple drawbacks. Oxygen plasma treatment is a time sensitive single attempt process, with the effect of the treated surface lasting only minutes. Moreover, it requires the use of an oxygen plasma machine, which has limited chamber size and is expensive. Bonding microfluidic devices using oxygen plasma is also a permanent process, but there are circumstances where having a

reversible seal is advantageous as well. While this may not be as desirable in wearable applications, having a reversible seal would be advantageous in harvesting cells or tissue sample.

Generally, methods for creating irreversibly or reversibly bonded microfluidic devices tends to be expensive in time and cost. Furthermore, the current ubiquitous method, plasma bonding, makes it more difficult to fabricate multilayer chips due to the time constraint and limited room for error. Having a simple fabrication method would provide more versatility and access for device fabrication and could potentially make commercialization possible.

This chapter introduces a simple method for creating reversible or irreversible bonding that does not require the use of specialized equipment.[47] This method uses a novel mixture of traditionally used PDMS and a silicone based soft skin adhesive (MG 7-9850) to create a cured polymer that still has adhesive properties. A temporary, reversible bond could be achieved with a glass slide, and a permanent irreversible bond could be achieved with further heat treatment. Using this method, we found the burst pressure of the fluidic device, demonstrate its biocompatibility with human heart cells, and fabricated a 3D fluidic chip construct.

5.2: Background

The ubiquitous method for bonding microfluidic devices is to oxygen plasma treat the surfaces before placing them in contact with each other. During an oxygen plasma treatment, the Si-CH3 bonds on the PDMS and glass is replaced with Si-OH groups, when the surfaces come in contact with each other, the -OH groups create to form Si-O-Si bond between the glass and PDMS. This same process can be done between PDMS and PDMS as well. Unfortunately, this process is time sensitive and requires specialize equipment, making it difficult to scale. Thus, researchers have developed other methods for reversibly and irreversibly sealing microfluidic devices.

There has been a variety of methods developed for irreversibly sealing microfluidic devices. Popular methods include corona treatment, using partially cured PDMS, or chemical based bonding. However, there is limited research for creating reversibly bonded microfluidic devices. Thomson et al. created a strong reversibly bond between PDMS based microfluidic devices and a glass slide using commercial double-sided tape. Shiroma et al. reported a simple process by sandwiching the microfluidic device between to glass slide and PDMS. While these methods are effective for single layer devices, they have not been proven for fabrication of more complex chip design such as multilayer chips or chips with functionalized surfaces for cell culture application.

5.3: Methods

5.3.1: Creating the Adhesive Silicone Polymer (ASP)

The adhesive silicone polymer is a mixture of traditional PDMS (Sylgard 184, Dow Corning®) and a two-part FDA approved silicone-based skin adhesive (MG 7-9850, Dow Corning®). The PDMS was first mixed at a 1:10 ratio of crosslinker to base by weight, and then the soft skin adhesive was separately mixed at a 1:1 ratio by weight. The ASP was formed by mixing the uncured PDMS and the uncured soft skin adhesive at a 1:40 ratio respectively by weight. The uncured ASP was then either poured into an acrylic microfluidic mold or spun coat onto a glass slide and cured for at least 2 hours in a 60^{O} Celsius oven.

5.3.2: Burst Pressure Test

To understand the strength of the seal for the reversibly and irreversibly sealed devices, a burst pressure test was used to determine the failure point of the bond. Three different bond conditions were examined: PDMS device adhered to a clean glass slide with no plasma treatment (control), adhesive silicone polymer device adhered on clean glass slide (reversible bond), and PDMS device adhered onto adhesive silicone polymer substrate (irreversible bond). The geometry used for the device was a 3 mm diameter chamber adhered over an inlet hole drilled through the substrate. For each test, the pressure within the chamber was increased incrementally until failure occurred.

Figure 5.1 shows the fabrication process for creating the reversibly seal and irreversibly sealed microfluidic device. The master mold for the device was created by placing a 3 mm diameter circle cut from Frisket Film (Grafix®) onto a flat and clean poly(methyl methacrylate) (PMMA) surface. PMMA walls were then cut using a laser cutter (VLS 2.30, Universal Laser®) and

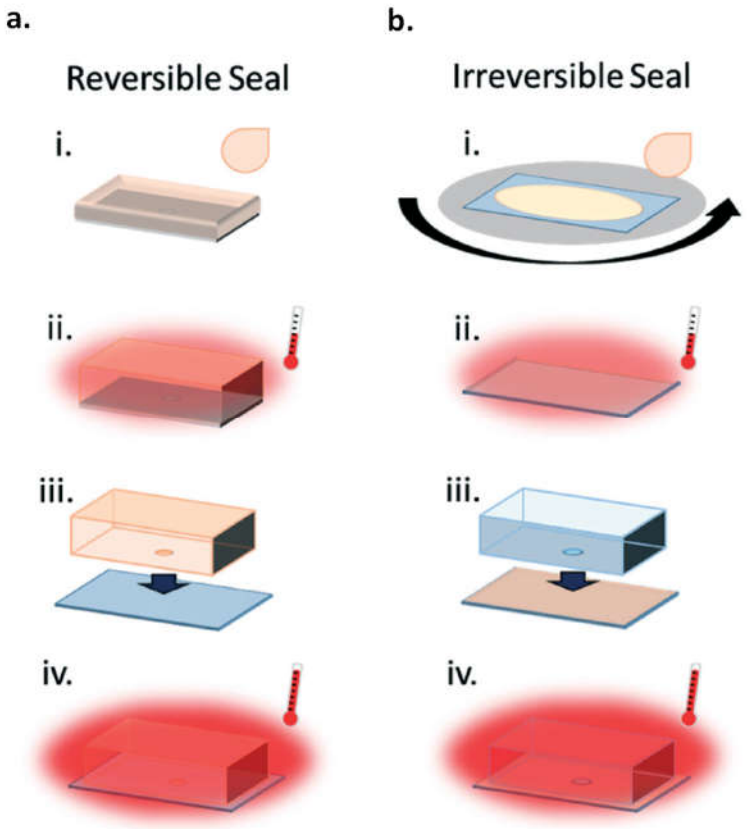

Figure 5.1. (a) The fabrication process for the reversibly sealed microfluidic device. (i) The master mold was first molded with the ASP. (ii) afterwards it was cured in the oven. (iii) The ASP was then demolded and placed on a cleaned glass slide. (iv) The entire construct was then bonded in the oven at a higher temperature. (b) The fabrication process for the irreversibly sealed device. (i) The ASP was first spun coat onto a cleaned glass slide. (ii) The ASP on the glass slide was then cured in the oven. (iii) A PDMS molded device is then placed on the cured ASP on the glass slide. (iv) The entire construct is then baked in the oven at a higher temperature.[47]

glued around each chamber to form levees to contain the polymer. Afterwards, either PDMS or ASP was poured into the molds and degassed for 15 minutes. The polymer was then cured in a 60^{O} Celsius oven for at least 3 hours.

The glass substrates for the devices were prepared by first cleaning 25 mm by 75 mm glass slides with isopropyl alcohol. After drying, scotch tape was then used to remove any debris on the glass slide, and inlet holes were drilled through the center of each glass slides. For the

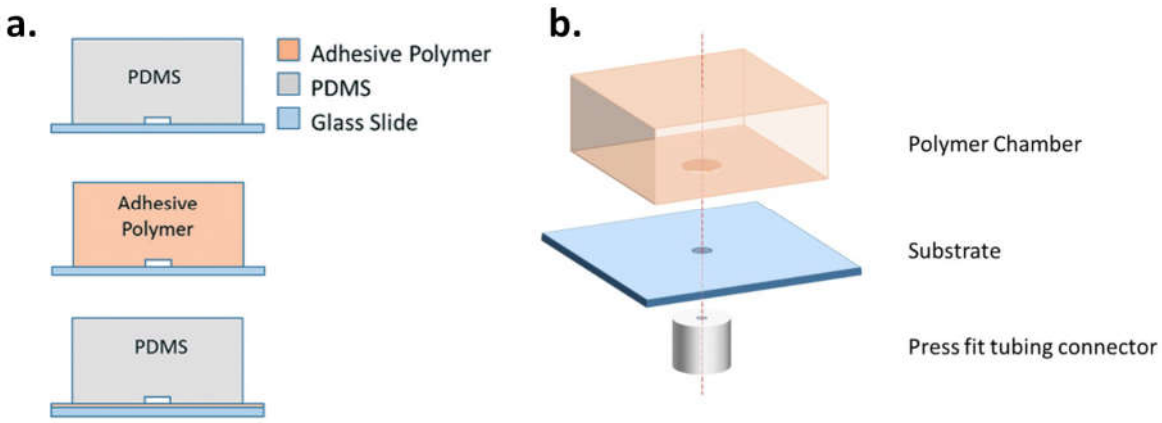

Figure 5.2. (a) The bond parameters tested. (b) The different layers for device assembly.[47]

irreversibly bonded devices, a layer of the ASP was spun coat over the glass slide at 800 rpm for 60 seconds. After curing, any debris in the inlets were removed. Finally, commercially available press fit tubing connectors (Grace Bio-Labs, Inc) was adhered on the glass slide opposite of the surface of the polymer device.

The device was assembled by placing the polymer device chamber side down on the substrate such that the chamber was centered over the drilled hole (figure 5.2). Slight pressure was applied to ensure a good seal and then the devices were placed in an oven at 120^{O} Celsius for 90 minutes.

For the testing, a flexible tube was inserted through the tubbing connector on the glass slide. The line for the tube was then split between a digital manometer (Dyer Series 490) and a syringe controlled by a syringe pump. The pressure of the system was gradually increased in a stepwise fashion by incrementally decreasing the syringe volume by 0.5 ml. The stable pressure was recorded for each step until failure occurred; failure was defined as an immediate drop in pressure to atmospheric pressure.

Reusability was also examined for the reversibly bonded devices. After each burst test, the ASP devices were carefully removed from the glass slide. Both the glass slide and device were washed using isopropyl alcohol and dried in a 60^{O} Celsius oven for 30 minutes. The glass slides and the ASP devices were then cleaned using scotch® tape 3 times before they were retested.

5.3.3: Single-Layer Reversibly Bonded Device Fabrication

Single layer fluidic chips were fabricated using the reversible and irreversible bonding scheme. For the reversibly sealed microfluidic devices, the ASP was used to mold a gradient generator design. The master mold for the gradient generator was fabricated using the Shrinky-Dink procedure first developed by Grimes *et al.* A laser printer was used to print the gradient generator design on to pre-stressed polystyrene (PS). The PS was then shrunk in an oven at 160^{O} Celsius. During the shrinking process, the heat will cause the ink to reflow while also shrinking the design. This will cause the ink to create channels. An acrylic levee was then glued around the design, and then the ASP was poured into the mold. After the ASP cured, and additional layer of PDMS was added and cured on top for additional support. Inlet holes was then punched, and the entire device was placed chamber side down onto a cleaned 25 mm x 75 mm glass slide. The entire construct was baked at 120^{O} Celsius for 90 minutes. The channels for the microfluidic chip was primed using ethanol before blue and yellow dye was flowed through.

5.3.4: Multi-layer Reversibly Bonded Device Fabrication

A multilayer, irreversibly bonded, micromixer was fabricated by bonding alternating layer of PDMS and ASP molded chambers together. The master mold of each layer was fabricated using Frisket Film laminated onto a clean acrylic surface. A laser cutter was used to cut the outline of the channel and chamber through the Frisket Film only, and the excess Frisket Film around the

channels were removed leaving only the positive channel structure. acrylic levees were added around the channels. Afterwards, either the ASP or PDMS was used to mold the channels and cured at 120^{O} Celsius for 2 hours. Once completely cured, inlet and outlet holes were punched into the different layers. The different layers were then assembled sequentially on a cleaned 50 mm by 75 mm ASP coated glass slide with the ASP molded layer in between the PDMS molded layer. The entire construct was then baked at 120^{O} Celsius for 90 minutes. The channels for the microfluidic chip was primed using ethanol before blue and yellow dye was flowed through.

5.3.5: Characterizing Polymer Swelling

PDMS will have different swelling properties when exposed to different types of solvents. Because the ASP is also silicone based, it is conceivable that it will also have different swelling behavior in different solvents. Thus, in order to better understand how ASP expands in different solvents a swell test was performed by placing the polymer in different solvents for 24 hours.

Solid cubes of PDMS and ASP were first made by casting the polymers in acrylic molds. The PDMS and ASP were both cured at 60^{O} Celsius for two hours. Afterwards, the cubes were removed from the molds and submerged in different solvents for 24 hours. A picture of the submerged cubes was taken right before and 24 hours after submersion. A scale bar was present in both pictures. ImageJ was then used to measure the length of the top surface of each cube before and after submersion. The average change in length for each set of cubes were calculated for the different solvents, and a t-test was used to determine any significant differences between the PDMS and the ASP.

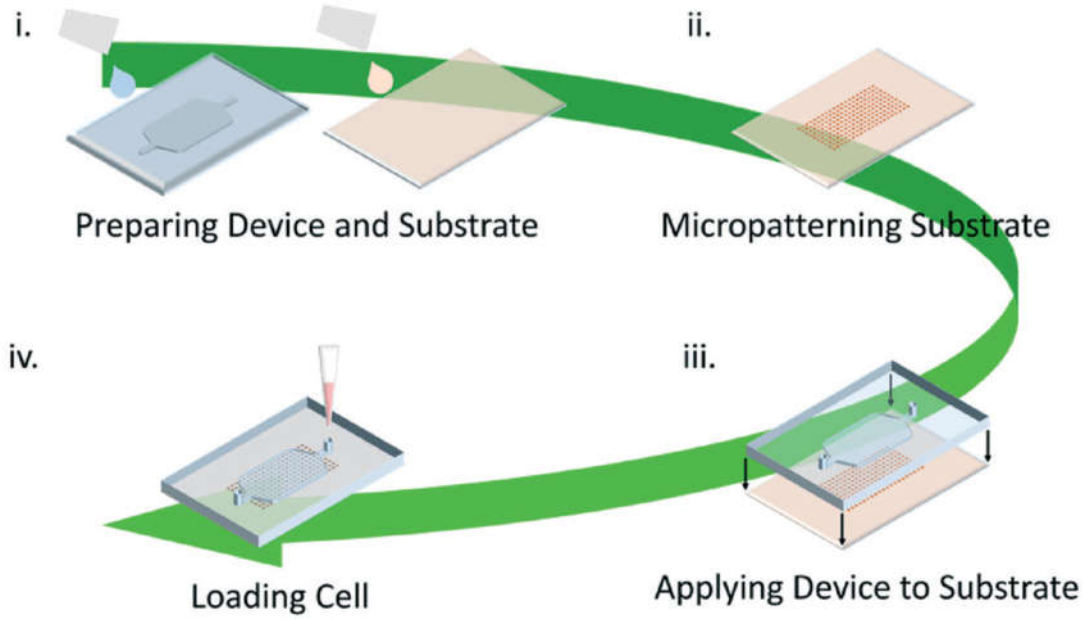

Figure 5.3. (i) A PDMS chamber was first fabricated. A glass slide was also covered with ASP and cured. (ii) An array of square islands of proteins was then selectively patterned onto the surface of the ASP covered glass slide. (iii) The PDMS chamber, with punched inlet and outlet holes, was then placed over the ASP. The entire construct was sterilized in the autoclave, which also help bond the device. (iv) Cells were then loaded into the PDMS chamber.[47]

5.3.6: Cell Patterning and Culture in Irreversibly Bonded Chamber

A larger irreversibly bonded fluidic chamber was fabricated for culturing human stem cell-derived cardiomyocytes (hES2-7E). Figure 5.3 shows the fabrication process for the chamber. A large fluidic chamber, with a height of 1.52 mm) master mold was created using PMMA. PDMS was used to mold the chamber and cured at 60^{O} Celsius for 2 hours. Uncured ASP was spun coat onto a 50 mm x 75 mm glass slide using the protocol described above and allowed to cure. Next, patterned islands for cell adhesion was then created on the surface of the ASP covered glass slide. A shadow mask of individual squares was cut and adhered onto the ASP covered glass slide. The surface was then treated using oxygen plasma for 3 minutes, and the entire slide was immediately placed in a 20% solution of 3-glycidoxypropyl-trimethoxysilane (GPTMS) in

methanol. The ASP covered glass slide was then washed, and the PDMS chamber was placed chamber side down over the patterned ASP covered glass slide. The entire construct was then autoclaved, which helps form the irreversible bond, and Matrigel (Corning ®) was flowed through the chamber to create the protein islands for the cells to adhere too. Cardiomyocytes were then loaded into the chamber and health was monitored. The contractility of the cells was assessed using an optical flow-based method. Principal component analysis (PCA) was used to summarize the data from the optical flow into a single vector. The contraction and relaxation event of the cells can be identified in the vector and plotted over time.

5.4: Results and Discussion

5.4.1: Material Properties

The soft skin adhesive (MG 7-9850) is an FDA approved platinum catalyzed silicone-based elastomer. Literature reported that this material is similar to the structure of PDMS.[48] The soft skin adhesive alone is incredibly soft and tacky, but by introducing small amounts of PDMS, the stiff and tackiness of the material is increased and reduced respectively. In this paper, we found the optimal ratio of PDMS to the soft skin adhesive to be a 1 to 40 in terms of adhesiveness and stiffness. However, the ratio could be adjusted for future work.

There were no significant differences in terms of swelling between the ASP and PDMS (figure 5.4). The number of solvents chosen for this test is not comprehensive, but they represent some of the most commonly used solvents in a standard laboratory and for cell culturing. The

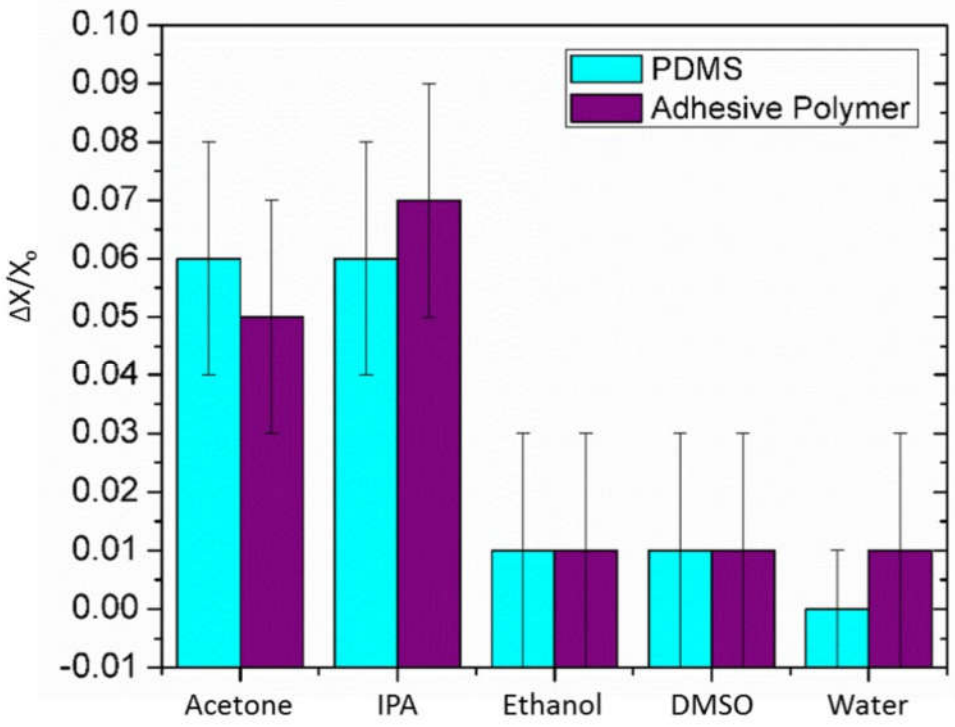

Figure 5.4. The different degree of swelling for the PDMS and the adhesive polymer in different solvents.[47]

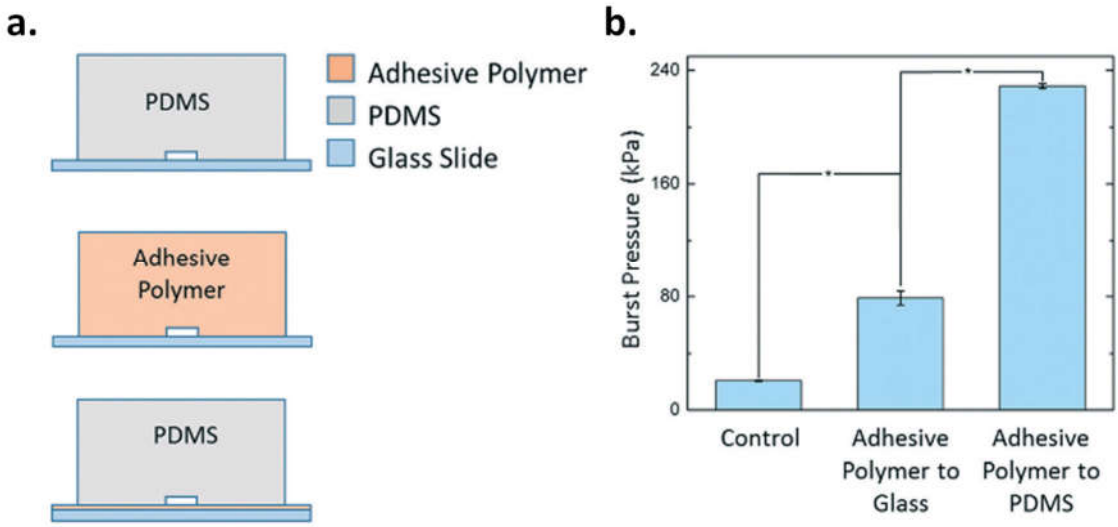

Figure 5.5. (a) The different types of bond formed. The PDMS to glass slide is the control; the adhesive polymer to the glass slide forms the reversible bond; the PDMS to the adhesive polymer on the glass slide forms an irreversible bond. (b) The burst pressure of each of the conditions in (a).[47]

most significant swelling occurred with acetone and isopropyl alcohol. DMSO, ethanol, and water all seemed to have little to no swelling. More importantly, there was minimal swelling with water, which is the primary solvent that most cell based, or wearable based devices will be in contact with.

5.4.2: Reversible versus Irreversible Bonding

Reversibility of the bonding depends on what material the ASP is bonded to. If the ASP is bonded to an untreated glass surface, then a reversible bond will form. This bond strength, however, can be improved with increased and prolonged temperature treatment. Figure 5.5 shows the burst pressure of the different conditions tested. The bond between the adhesive polymer and the glass failed at 79 ± 5 kPa; this is about four times more than the failure of just the PDMS and glass, which occurred at 21 ± 1 kPa. Even though there is a higher bond strength, the failure of the device did not harm the footprint of the chamber. Moreover, the devices could

Table 5.1[47]

Trial	**1**	**2**	**3**
Burst Pressure (kPa)	79 ± 5	76 ± 4	77 ± 3

still be reused, after washing and re-bonding, with minimal lost in bond strength, as seen in table 5.1. This bond strength is enough for common microfluidic tasks such as gradient generating, droplet generation, and cell culturing; a gradient generator was demonstrated using this method, with subsequent removal of the device demonstrated in figure 5.6.

An irreversible bond can form when the ASP is bonded to a PDMS surface at high temperature and for a prolonged period. Sia *et al.* defined an irreversible seal with a bond strength that can withstand pressures ranging from 207 to 345 kPa. The bond strength between the ASP and PDMS reached a pressure 229 ± 2 kPa before the manometer reached its limit. Thus, it is unclear what the maximum pressure the bond between the ASP and PDMS can handle, but it is within the range of pressure defined for an irreversible bond. Moreover, removal of the

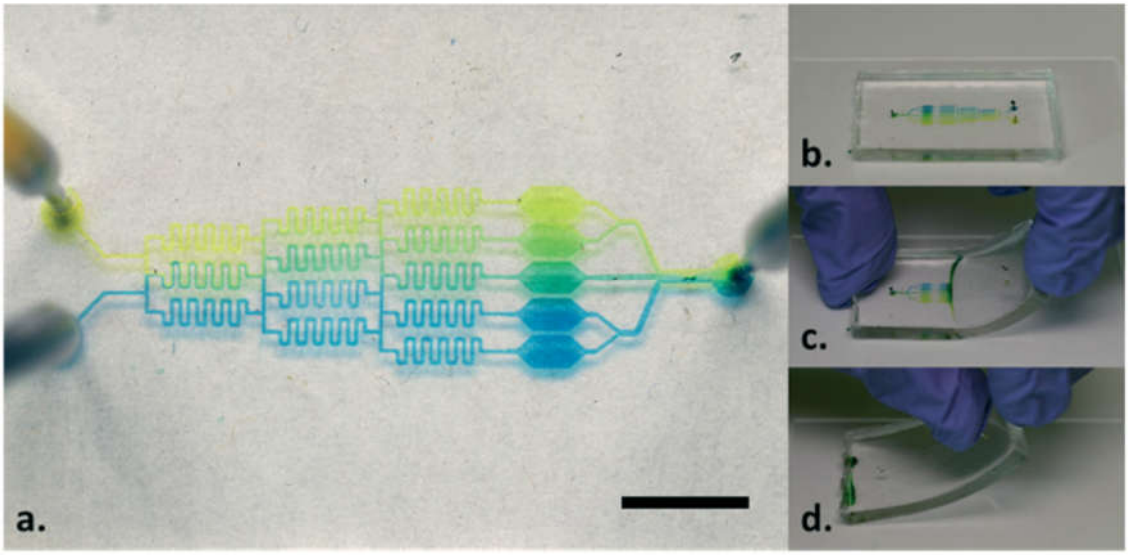

Figure 5.6. (a) Image of the microfluidic gradient generator fabricated using the reversible bonding scheme. (b-d) The removal process of the microfluidic gradient generator device.[47]

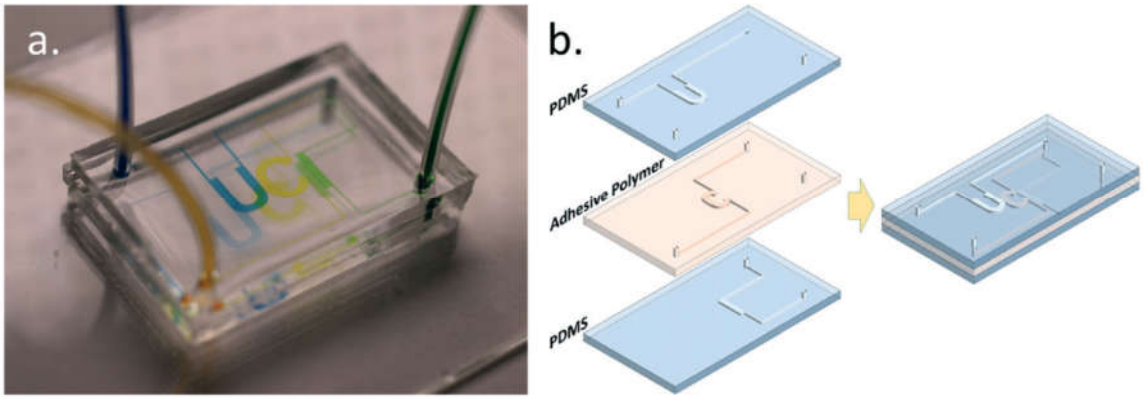

Figure 5.7. (a) Picture of a three-layer microfluidic mixer. (b) The exploded view of the different layer of PDMS and adhesive polymer.[47]

chamber resulted in tearing of the ASP layer; however, the PDMS device component was left intact. We believe because the ASP is much softer than the PDMS, any tensile stress applied to remove the device will result in the ASP tearing before the PDMS does. While this removal method results in the destruction of the device, it still provides a controllable way to disassemble the device by using the ASP as a sacrificial layer.

A multilayer microfluidic mixer was also fabricated by alternating layer of molded PDMS and molded ASP (figure 5.7). The fabrication of the multilayer device was relatively simple because there was no constrain on time or the number of tries for aligning each layer of the device. Each layer of the device was aligned multiple times before the irreversibly bond between each layer was formed in the oven. There was successful mixing of the blue and the yellow dye to form the green in the third layer.

5.4.3: Compatibility with Cells.

We demonstrated the ability to micropattern as well as culture Human stem cell-derived cardiomyocytes on top of the ASP. A large array of square protein islands was successfully created by selectively functionalizing the surface with GPTMS and bonding protein to the surface. The

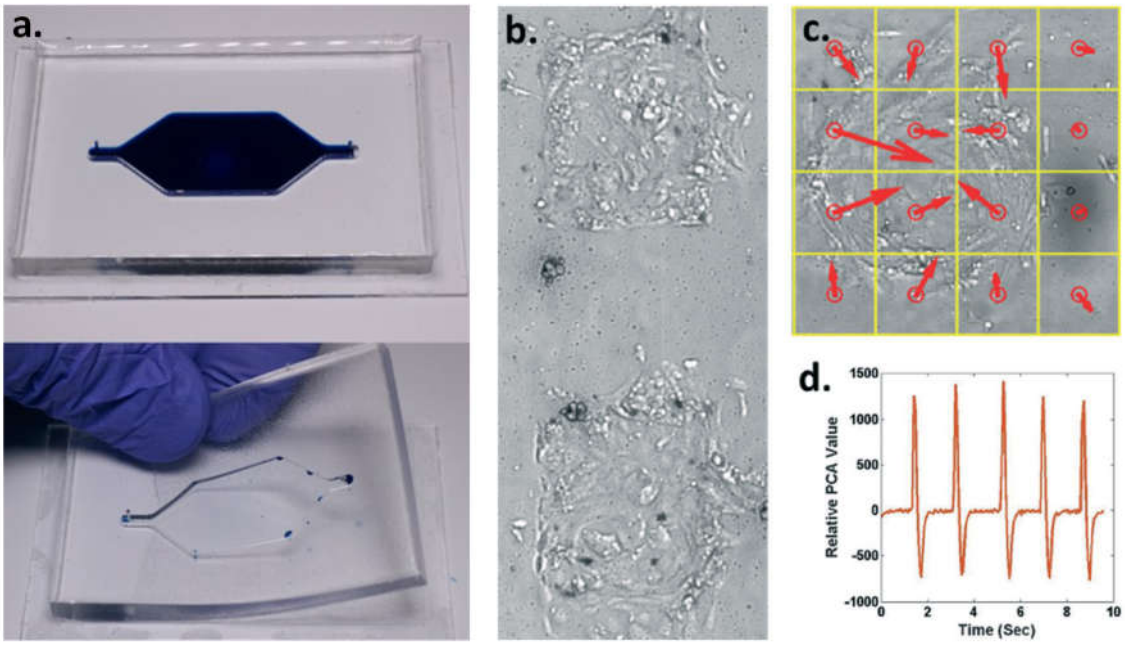

Figure 5.8. (a) An image of the irreversibly bonded fluidic chamber (top) and the removal of the chamber from the ASP (bottom). The removal of the chamber tore the layer of adhesive polymer bonding the PDMS chamber. (b) Brightfield image of the square islands of cardiomyocytes. (c) The motion vectors of a single square island of tissue found using optical flow method. (d) The first principal component of the optical flow signal from (c).[47]

patterned area was larger than the dimension of the chamber; however, a strong seal was still achieved over the excess islands along the border of the chamber. This provided a larger tolerance for alignment of the device. Moreover, as mentioned above, removal of the PDMS chip was controlled, with the ASP substrate acting as a sacrificial layer and ripping, while leaving the chamber portion intact (figure 5.8).

Human stem cell-derived cardiomyocytes were successfully cultured on the ASP. The cells grew on the patterned areas and exhibited contractions within the second day after seeding. Figure 5.8 shows the islands of cells, with the motion vector generated from the optical flow method, and the summarized vector from the PCA. The cells in the chamber were viable past 150 days. This suggest that there was minimal leeching of any cardiotoxic chemical. While this does

not definitively prove biocompatibility, it does suggest that this material does not have any immediate harmful effect.

Cells tend to be very dynamic and complex systems that are very sensitive to their environment. Thus, there are multiple factors that needs to be accounted for when using the ASP to grow cells. One of the primary parameters that needs to be examined is the stiffness of the substrate used to grow the cells. The ASP is much softer than PDMS, so it is conceivable that the stiffness will have some effect on the growth of the cells. Moreover, while we did demonstrate successful growth of cells on the ASP, more work needs to be done to determine the compatibility between this material and other cell types, as well as any potentially harmful chemical from leeching.

5.5: Conclusion

5.5.1: Summary

We have demonstrated a new scheme for creating reversible and irreversible bonds for microfluidic devices using a novel adhesive silicone polymer. This polymer is a ratio between traditional PDMS and a silicone based soft skin adhesive. A reversible bond is created when the cured ASP is placed on glass, and an irreversible bond can be achieved by placing the cured ASP directly on PDMS. Because bonding between the two material is not time sensitive or limited to a single try, there can be multiple attempts at fabricating the microfluidic devices if proper alignment between the substrate and device is not achieved on the first try. This method is more forgiving compared to the traditional microfluidic bonding using oxygen plasma, which is a time sensitive process that normally only allows a single attempt before the effect of the oxygen plasma wears off.

We also demonstrated multiple applications including the fabrication of a reversibly bonded gradient generator and irreversibly bonded 3-layer micromixer. Additionally, we were also able to selectively micropattern proteins on the ASP and demonstrated the material's compatibility with human stem cell derived cardiomyocytes with cell viability lasting past 150 days. While these studies are still preliminary, it suggests that this material has the potential to be integrated with traditional PDMS device fabrication. PDMS devices could potentially be built on ASP coated glass slides, instead of having to rely on oxygen plasma, to achieve an irreversible bond. This would eliminate the need for specialized equipment such as an oxygen plasma machine and makes microfluidic fabrication more accessible.

5.5.2: Integration with Wearable Systems

Fundamentally, we have developed a material that can create a reversible bond with glass and an irreversible bond with PDMS. While this type of material may have great potential in microfluidic manufacturing, it can also be applied towards fabricating wearable sensors. There are already work done in literature that uses PDMS devices to collect and analyze sweat off of human subjects.[46] Much of these processes still uses oxygen plasma to fabricate the device, which makes scaling difficult. Devices in the future could potentially be laminated together using the ASP as a bonding layer. Moreover, because the ASP is created from an FDA soft skin adhesive, application of the adhesive to the device could potentially be an alternative bonding scheme between the device and the skin.

Chapter 6: Integrating Surface Mounted Technology with Stretchable Circuits

6.1: Introduction and Motivation

Soft stretchable electronics (SSE) can operate in highly irregular, curvilinear, and dynamic environments that traditional printed circuit boards (PCBs) normally cannot. Fields such as soft robotics, where the uniqueness of the system is in the inherent flexibility and softness of the robots, would benefit from integrating soft electronics instead of conventional hard PCBs. SSE also integrates better with environments such as the human skin, providing more comfort as well as high quality signal under dynamic environments.

While there is ongoing research in creating stretchable electronic components, such as transistors, etc., the work in this area is still immature. However, the current electronic and wireless infrastructures are built on these electronic components, generally in the form of surface mounted devices (SMD). Thus, in order to have functional SSE that is compatible with the wireless and electronic infrastructure, there is a need to integrate these traditional surface mount passive and active components with the soft stretchable electronics.

In this chapter, we introduce a method for integrating SMD with the highly stretchable wrinkled metal thin film interconnects previously developed by Khine lab. The introduced method specifically controls the distribution of strain around the interface of the SMD and the wires using rigid nylon meshes of different geometries. An indentation into the mesh is placed at the interface of the nylon mesh and the interconnect; this “cove” like geometry serves to help prevent any large deformation from occurring at the interface between the interconnect and nylon mesh. We demonstrate the effect of the rigid island nylon mesh in the delaying of the

failure points of the soft stretchable electronics. Moreover, we also show the successful integration of different types of SMD, with applications ranging from simple circuit design to the integration of photodiodes and LEDS with a highly stretchable strain sensors used for respiration and pulse monitoring.

6.2: Background

Soft stretchable systems that integrates traditional SMDs with soft interconnects can be divided into three parts. The first part is the type of SMD that will be used. Because surface mounted technology (SMT) is very mature, there is very little variability in this type of technology since all components have standardized parts, tolerances, and units. The second component is the interconnect between the SMD. These interconnects form the soft, stretchable circuit that the SMD will be mounted on. There has been much research in creating stretchable electronics, and there exist many different schemes for making flexible and stretchable wires. The last, and the most important, part is the conductive interface between the SMD and the wires. This is directly responsible for the quality of the integration between the SMD and interconnects and is often the first failure point in the system.

One of the major hurdles that must be overcome when integrating SMDs with soft electronics is the interface between the two systems. SMD are hard brittle components with very high young's modulus; contrastingly, soft electronics are very flexible with very low young's modulus. When the two are paired together, there is a large mismatch in modulus between the materials, resulting in regions of high stress concentrations at the interface. Areas of high stress concentration are the primary failure points during mechanical deformation. Consequently, it is important to minimize the stress concentration in these areas to prevent premature failure of the joint from fatigue.

Chapter 3 of this dissertation explored the different methods reported in literature for creating stretchable and flexible electronics. These methods include creating conductive polymer, liquid metal wires, and metal thin films with strain relieving structures. The different

schemes used to integrate SMD with soft stretchable interconnects were also reviewed as well. Researchers have explored methods ranging strain isolating islands to direct integration of the SMD onto an electronic substrate with comparable stiffness. Regardless of the material and method used, the end result always involves minimizing or delocalizing the stress concentration between the SMD and stretchable wire interface. This prevents any large concentration of stress that may lead to premature cracking and failure at the interface.

6.3: Methods

6.3.1: Integrating the Nylon Island Mesh, SMD, and Stretchable Gold Wire

The fabrication of the stretchable interconnect follows the protocol created by Kim *et al*. described in chapter 4.[42] For the stretchable circuit specifically used in this work, 40 nm of gold was used to create the wrinkled metal thin film interconnects. The interconnects have a width of .4 mm and is bonded to a silicone elastomer substrate (Ecoflex) that is about .5 mm thick. The dimensions of the substrate varied between 4 to 15 mm depending on the circuit design. Different circuit designs were created for different applications (figure 6.1).

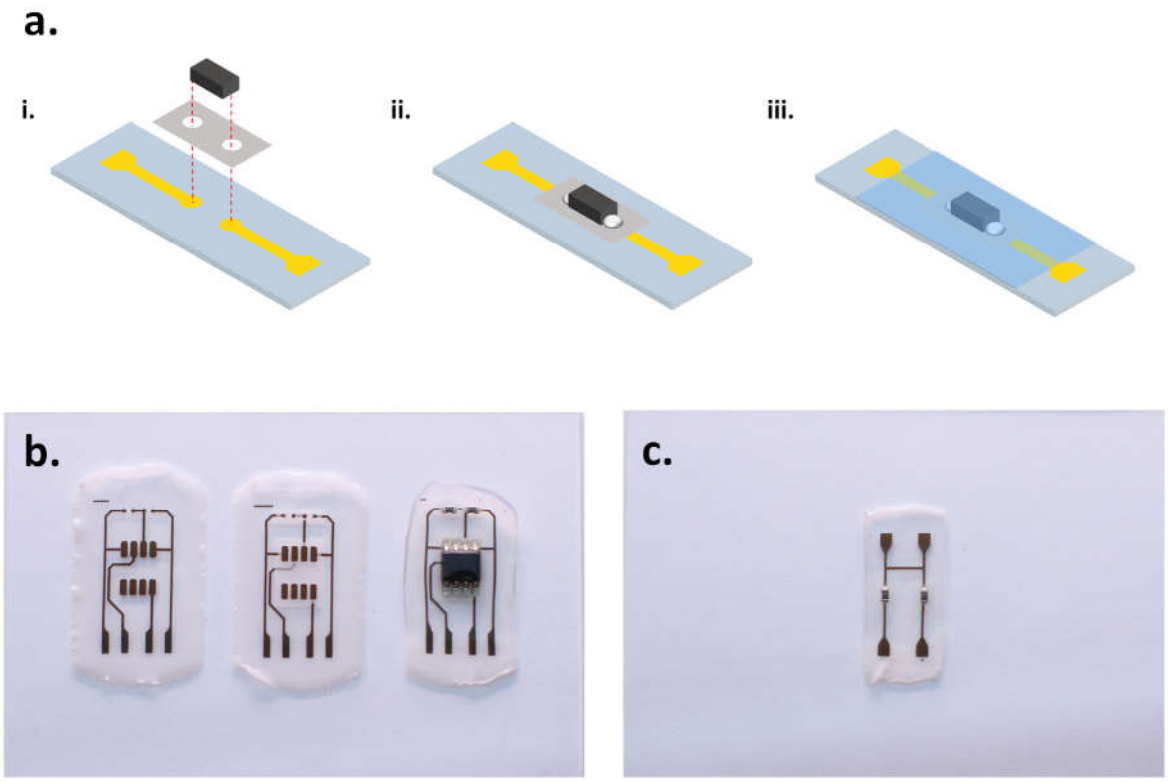

Figure 6.1. (a) The integration scheme for attaching the SMD onto the stretchable circuit. (i) The SMD, nylon mesh island, and stretchable circuit are aligned. (ii) The SMD is attached onto the stretchable circuit through the holes of the nylon mesh islands using conductive epoxy. (iii) After the epoxy cures, a layer of Ecoflex is applied to encapsulate the circuit. Connection pads are left exposed. (b) The different steps of attaching the SMD is shown for an operational amplifier circuit. (c) Picture of the design used for a voltage divider and RC circuit.

The soft stretchable circuit was fabricated with four distinct layers to it. The bottom layer is the stretchable interconnect in Ecoflex. The next level is the nylon mesh, which is selectively placed over the interconnects, and the third level consists of the SMD placed on top of the nylon mesh. Conductive silver epoxy is used to adhere the SMD, through holes cut in the mesh, onto the interconnects. The fourth and final layer is another layer of Ecoflex to encapsulate the entire construct. The overall integration of the different levels can be seen in figure 6.1a.

The geometries for the nylon mesh was fabricated using a laser cutter to cut the design directly into the mesh. After the mesh was placed over the interconnect, a paper mask was used as a shadow mask to selectively apply the conductive epoxy through the holes and onto the interconnect. After the epoxy was applied, the mask was removed, and the SMD was placed on the epoxy. The device is then placed in a 60^{O} Celsius oven and the epoxy is cured for 2 hours. After the epoxy has curd, the entire sensor is encapsulated, except for the contact pads, in another layer of Ecoflex via spin coating at 500 RPM for 35 seconds.

6.3.2: Island Mesh Geometry Testing

To determine the effect of the cove depth on the strain delocalization, island mesh with different cove depths were constructed (figure 6.2). Resistive SMD with a resistance of 1 kΩ was

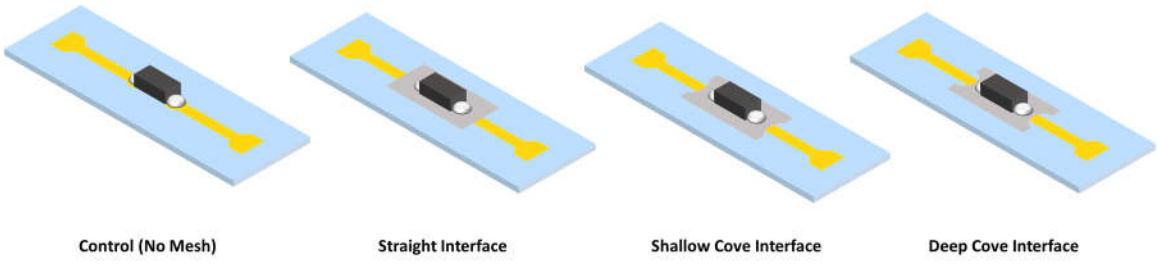

Figure 6.2. The different mesh geometries tested. The left is the control with no nylon mesh used. The straight interface (second to the left) used a 2 mm by 4 mm mesh geometry with a straight interface. The shallow cove interface (third from the left) contains a .25 mm deep arche into the nylon mesh at the interface between the interconnect and the mesh. Lastly, the deep interface (fourth from the left) has a .5 mm deep semicircle at the interface between the mesh and the interconnect.

mounted through the mesh onto a straight interconnect design. The Ecoflex substrate had dimensions of 4 mm by 16 mm. There was a total of 3 mesh geometries and a control that was assessed. The control device had the SMD attached directly onto the interconnect with no nylon mesh. The first of the mesh design used was a 2 mm by 4 mm rectangular geometry with a straight interface between the mesh and the interconnects. The second design incorporated a shallow cove into the rectangular geometry at the interface between the nylon mesh and the interconnect; the cove had a depth of .25 mm. The final design used a deeper cove with a depth of .5 mm. Each device was stretched lengthwise until failure.

6.3.3: Stretchable Circuit Testing

A variety of different circuits were fabricated using the nylon mesh islands as strain relief structures between the SMD and the interconnects. First, simple passive surface mounted components were attached to the straight trace geometry to understand the behavior of the device under strain. Following the same fabrication procedure stated above, a set of circuits with simple straight interconnects was created using 330 kΩ surface mounted resistors and 330 pF surface mounted capacitors. The shallow cove nylon mesh design was used. The substrate dimension was 4 mm by 10 mm, and the entire circuit was stretched lengthwise by 6 mm.

Slightly more complex circuits were also fabricated. The first stretchable circuit made was a resistor capacitor (RC) circuit with a 1 kΩ resistor and 100 µF capacitor. The shallow cove geometry was used for the RC circuit. Next a voltage divider with 51 kΩ resistor components and a non-inverting amplifier with 31 kΩ circuit components were created. The operational amplifier had a gain of 2. Both of these circuits were constructed using both the shallow and deep cove geometry. The RC circuit and voltage divider circuit had a substrate dimension of 10 mm by 18

mm, and the operational amplifier circuit had a dimension of 15 mm by 18 mm. All circuits were stretched a total distance of 6 mm.

6.3.4: Integrating SMD with a Soft Stretchable Strain Sensor

Pegan et al. previously developed a highly stretchable strain sensor.[43] This sensor was used for measuring respiration, which will be described in chapter 7. An altered version of the strain sensor was designed so that it incorporated the stretchable interconnects for integrating and LED and photodiode for measuring pulse. Fabrication of the sensor followed the protocol listed in chapter 4. The different metal thin films were deposited in a step-wise fashion with 5 nm of platinum and gold being deposited first over the exposed strain sensor geometry of the polystyrene. Afterwards, the strain sensor portion was covered, and 40 nm of gold was deposited over the interconnect portion of the sensor. A green LED and photodiode were integrated into the sensor using the protocol described. Two sensors were fabricated and used to measure respiration and pulse concurrently on a human subject.

For the subject test using the PPG and the strain sensor, the respiration volume and ECG was measured using a continuous flow spirometer and single lead ECG connected to a BIOPAC data acquisition system. The strain sensors were also connected to the BIOPAC data acquisition system through a voltage divider circuit. The PPG was acquired through a custom amplification circuit attached to the National Instrument Data Acquisition System.

6.3.5: Finite Element Simulation

To better understand the distribution of strain around the nylon mesh, finite element analysis was performed for each mesh geometry and different substrate geometry using Ansys 2019. A hyperelastic Mooney Rivlin model was used to model the Ecoflex while the nylon mesh

was assumed to be an isotropic elastic material. The geometries in each finite element model (FEM) were taken up to 30% strain in the simulation, and the normal strain at the interface was used for analysis.

6.4: Results and Discussion

6.4.1: Nylon Mesh Island Geometry

The purpose of the nylon mesh is to move any large strain away from the conductive epoxy and interconnect interface. The epoxy and interconnect interface is a hard/soft connection point that will experience large amounts of strain. Accordingly, this interface should have the earliest failure point. The addition of a nylon island mesh will help stabilize the epoxy/interconnect interface and move any strain away from this junction. The nylon mesh itself is not actually in contact with the stretchable gold wire; rather, there is always a layer of Ecoflex between the wire and the mesh that helps buffer and protects the wire. While, the nylon mesh with the straight interface did remove the strain away from the epoxy wire interface, the strain is now concentrated around the nylon mesh and wire interface. The purpose of integrating the cove geometry around the wire interface is to further remove the concentration of strain from that interface. Naturally, the deeper the cove depth, the further the strain will be delocalized from the interface.

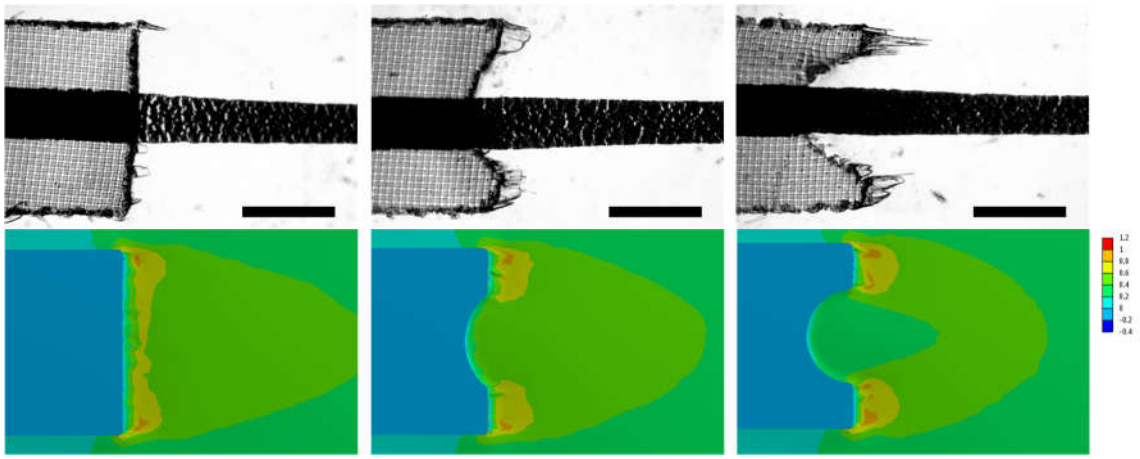

Figure 6.3. The top row shows the brightfield images taken of the nylon mesh and interconnect interface for different mesh geometry. The bottom row is the FEM, for each mesh geometry, displaying the normal strain over the stretched Ecoflex.

Figure 6.3 shows the different nylon mesh geometries and the associated FEA of the normal strain distribution at the interface between the interconnect and the mesh. Visually, the introduction of a cove structure will help delocalize the strain from within the cove itself. The top row of the figure is brightfield images taken at 2 times magnification of the interconnect and nylon mesh interface; The dark horizontal center line is the stretchable interconnect and the white defects in the lines are fractures in the film. As the cove depth goes from flat to deep, the fracturing in the film becomes less apparent. The deeper the cove structure, the less strain there is within the cove. Accordingly, we believe that this helped minimize the fracturing of the wrinkled metal thin film.

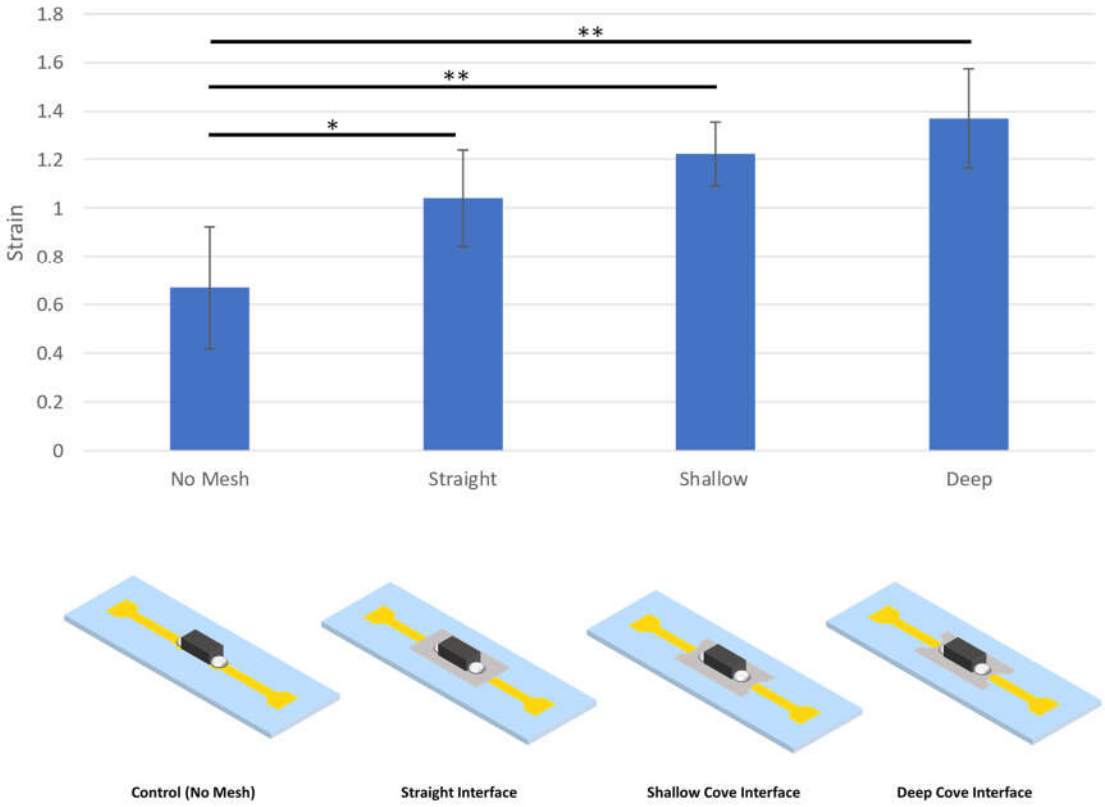

Figure 6.4. The failure strain of the different mesh geometries when pulled lengthwise. * indicates $p < .1$ and ** indicates $p < .05$

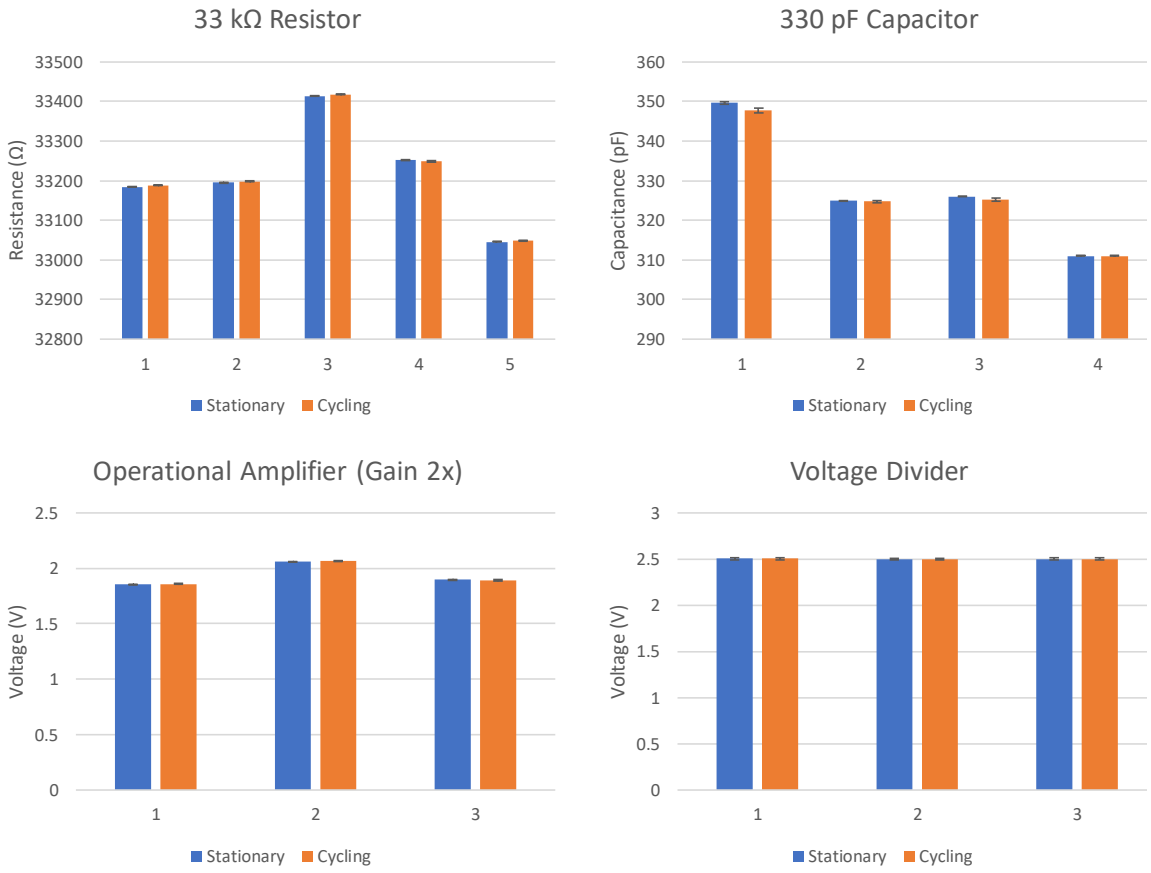

Figure 6.5. Bar graphs comparing the stationary and cycling average values for different sets of different circuit type. The operational amplifier and the voltage divider used the deep cove geometry while the resistor and capacitor used the shallow cove geometry.

The different mesh geometries were integrated with a 1 Ω resistor and a simple straight interconnect circuit. The circuit was pulled lengthwise until failure of the circuit occurred. The control used in this experiment had the SMD directly connected onto the interconnect with conductive epoxy without using a nylon mesh. Figure 6.4 shows the bar graphs of the failure strain for the different conditions. As expected, the control failed the earliest at a strain of 67% ± 25% standard deviation. Comparatively, the average strain at failure for the square nylon mesh, with no cove, was 104% ± 20% standard deviation. The average failure strain for the shallow and

deep coves were respectively 122% ± 13% standard deviation and 137% ± 20% standard deviation. There is a significant difference in adding the nylon mesh with the cove geometry. This result suggests that a shallow cove design, compared to the deep, would be enough to build a stretchable circuit that only needs to strain 60%, double what a stretchable circuit would generally experience on the body. To test this, several different types of SMD and stretchable circuits were built and tested using the shallow cove design.

6.4.2: Stretchable Circuit Performance with the Shallow Cove Design

Single surface mounted capacitor and resistor components were tested to determine the effect of strain on the SMD performances. The substrate geometry for each device was 4 mm by 10 mm, and each component was able to strain up to 6 mm, for a 10 mm initial length, with no failure (figure 6.5). An RC circuit was also built using the shallow cove geometry. The circuit was strained by 1 mm until a total of 6 mm was achieved; the original dimension of the circuit was 10 mm by 10 mm. The time constant for the system was calculated at each step up and each step down. There was no significant difference between each step for each sensor calculated as calculated by a one-way analysis of variance (figure 6.6).

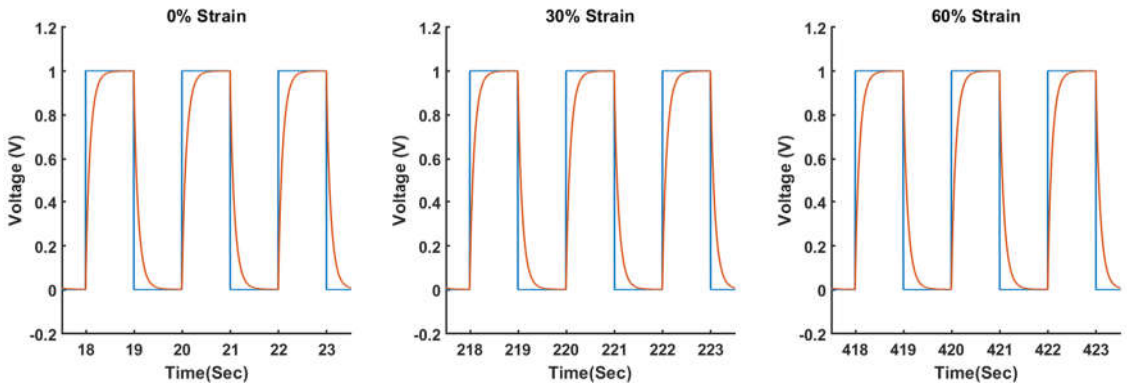

Figure 6.6. The RC voltage response for an alternating square wave with an amplitude of 1 volt. The RC voltage response is plotted for 0%, 30%, and 60% strain.

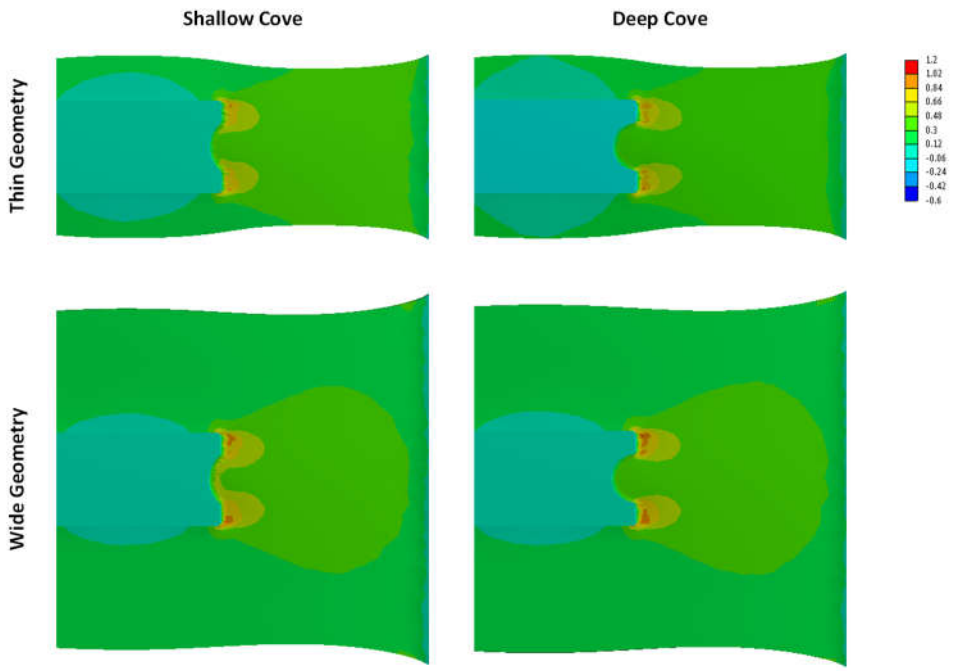

Figure 6.7. FEA of the normal strain for different nylon mesh geometry and different substrate dimensions

While the shallow cove geometry worked for the individual SMD components and the RC circuit, it did not work well for the voltage divider and operational amplifier circuit. For both systems, the device failed early between .1 to 1 mm of stretch, which is equivalent to or less than 10% strain. The performance was contrastingly different with the RC circuit, especially considering that they share similar substrate dimensions. Moreover, visual analysis showed high concentration of cracks around the interface between the nylon mesh and the wires.

To better understand the distribution of strain around the nylon mesh, finite element analysis (FEA) was performed to look at the normal strain distribution around the different mesh geometries with respect to the elastomer substrate dimensions (figure 6.7). With the FEA, it is visually apparent that the distribution of strain around the nylon mesh is affected by the geometry of the substrate. More specifically, as the substrate dimension aspect ratio decreases,

the strain will start to concentration again around the cove area of the mesh for a given stretch. For the same stretched length across all substrate dimensions, the mesh geometries with the deeper cove design had relatively lower concentration of strain around the cove. This effect, however, is not as apparent in the higher aspect ratio substrates. The finite element result in conjunction with the experimental results, would suggest that strain distribution around the island mesh is affected by both substrate geometry and mesh geometry. Moreover, because the fabrication process for the interconnect is still relatively manual, the inherent failure point of each circuit will be different, and the shallower mesh geometry may amplify the premature failure. This would explain for the discrepancy in between working and failed circuit that had similar substrate dimensions. According to the FEA, the deeper cove design will not be affected by the geometry change of the substrate as much as the shallow cove design.

6.4.4: Stretchable Circuit Performance with Deep Cove Design

A second set of voltage divider and operational amplifier circuit was designed with the deeper, .5 mm cove design. All circuit fabricated successfully stretched to 6 mm in length without failure. We believe that the deeper design helped delocalize the strain from the cove more robustly; moreover, the deeper cove may also allow for more leeway, in terms of failure point, with interconnects that was fabricated with less quality. For the voltage divider, there was no apparent change in signal between the stationary circuit and circuit cycled 20 times. For the operational amplifier, there was small changes in signal during the cyclic testing. This suggest that

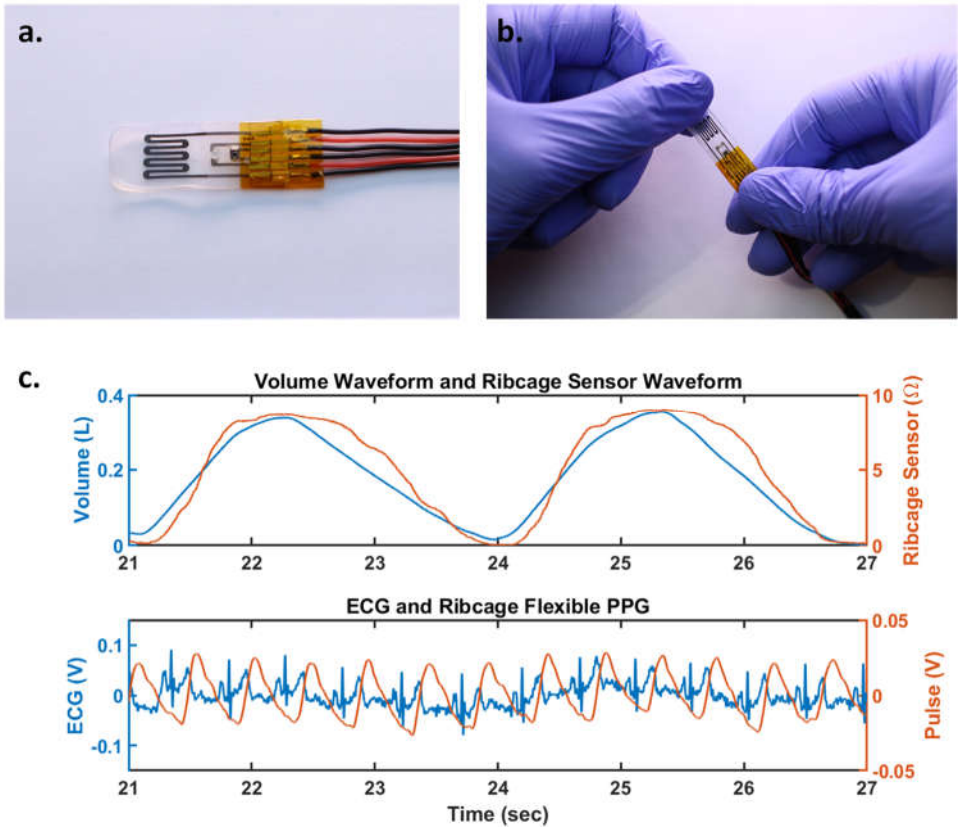

Figure 6.8. (a-b) Images of the stretchable strain sensor integrated with the photodiode and green LED. (c) Waveform of the measured respiration and pulse from the subject.

the interface created by the nylon mesh may not be entirely stable and further optimization may be required.

6.4.6: Integrating Respiration and Pulse Monitor

The strain sensor and PPG were successfully integrated to measure respiration and pulse simultaneously. Figure 6.8 shows pictures of the actual sensors as well as the waveforms for both the pulse and respiration. The PPG used an external amplifying circuit that was created on a perforated circuit board. However, future devices can potentially build the entire amplifying and filtering circuit on a single stretchable circuit. The pulse measurement was verified using ECG measurements that were taken concurrently. The respiration was verified using a continuous

spirometer that was measuring flow from the mouth while the strain sensor was measuring movement from the torso due to breathing. The sensors were placed on the abdomen and chest wall where both the PPG and the respiration signals were acquired.

6.5: Conclusion

6.5.1: Summary

We successfully integrated SMD with soft stretchable gold wires by introducing single layer strain relieving island geometries at the intersection between the SMD and the soft stretchable interconnect. The island is a nylon mesh with a “cove” type design that helps prevents large strains from forming at the interface between the mesh and the interconnect. The distribution of strain around the island is not only affected by the island mesh geometry, but also by the substrate dimensions. Deeper cove geometry needs to be used to provide enough strain relief for circuit substrate with lower aspect ratio. Using coves with a depth of .5 mm, we were able to stretch different circuit designs, including voltage divider and operation amplifiers up to 6 mm with no significant change in the output of the signal. Lastly, we successfully integrated SMD with a stretchable strain sensor to measure respiration and pulse concurrently.

6.5.2: Integration with Wearable Sensors

While this work is still preliminary, we demonstrated that the integration of different mesh geometries can help delocalize strain concentration between the SMD and interconnect interface. This increased the robustness of the circuit and may potentially be a viable method for integrating conventional SMD with soft stretchable electronics. Other strain relieving geometry could be used as well. Areas of no strain could be built into a stretchable substrate by inserting flexible stiff islands. Further study into the different cove geometry needs to be done, and verification of the finite element analysis should also be performed.

Future work should focus on integrating and entire wearable system on a stretchable circuit. This would include the circuit element as well as the active integrated circuit component

such as the microcontroller and battery. Additionally, the frequency response of the system should also be examined to make sure that the operation of the circuit is still acceptable within a set frequency range. If these conditions are achieved, then a truly soft stretchable circuit that can be integrated with current wireless infrastructure could be realize.

Chapter 7: Application of Soft, Wearable Sensors for Respiration Monitoring

7.1: Introduction and Motivation

Cardiovascular and respiratory diseases are among the top 10 disease that plagues the US[49]. Chronic respiratory disease (CRD) by itself is a growing global burden. Two common CRD, Asthma and chronic obstructive pulmonary disease (COPD), affect more than 435 million people worldwide and have an estimated annual cost of 50 billion dollars[50–52]. Cardiovascular disease (CVD) is also comparable in number of affected patients. It is estimated that the number of people affected by CVD will grow to be 132 million people with an estimated cost of 1.1 trillion dollars[53]. Given the impact and expected growth of these diseases, there is an undeniable need to continuously monitor these patients for early intervention to prevent exacerbation of any symptoms. Specifically, it is important to monitor the respiration health of the patients continuously.

In the previous chapter, we demonstrated that a pulse sensor could be integrated with the soft stretchable strain sensor used for measuring respiration. In this chapter, we report a method for measuring respiration rate and volume using only the strain sensors strategically placed on the body.[44] The chapter explains a method for calculating respiration rate, and more importantly volume, using small sticker like strain sensor placed externally on the skin above the chest wall and abdomen. We also demonstrate the application of this system on an ambulatory patient. The advantages and drawbacks of this system is also explained.

7.2: Background

The primary way for assessing respiratory health is through discrete tests called pulmonary function tests. These tests can range from simple spirometry to full body plethysmography for assessing simple airflow to assessing complete lung volume[54–56]. While tests such as PFTs are good at assessing a patent's respiratory health at discrete time points, they cannot continuously measure a patient's health continuously on a daily basis. Recent studies have shown that continuous measurement of respiration can help with patient respiratory health and recovery.[57] Continuous respiration monitoring for patient outside of a clinical setting has potentially large benefits.

There are different methods used for continuous, non-invasive ways of measuring respiration. Most of these methods relies on measuring the external volume of the chest wall and abdomen to back calculate the volume of air exchanged by the lungs. An early example used respiratory inductive plethysmography (RIP), which uses two inductive belts placed around the ribcage and abdomen to measure circumferential changes in chest wall and abdomen dimension during respiration.[58,59] Researchers in the late 1960's realized that the output from the bands had a linear relationship to respiration volume. Thus, using a multiple linear regression, a model could be created to calculate respiration volume using the changes in circumference from the chest wall and abdomen.[18,60–62] While this method works well on stationary subjects, bands used is bulky and moves easily, making motion artifacts a significant problem. This makes the band poor at measuring respiratory volume on a subject in an ambulatory environment.

Similar to RIP, optical and non-contact tracking of the chest wall and abdomen movement during respiration could also be used to calculate respiration volume. Optoelectronic

plethysmography (OEP) uses reflective balls placed over the chest wall and abdomen and multiple cameral to track the movement of the torso.[63,64] The 3D coordinate of each marker can be calculated, and the movement of those marker over time is recorded and used to calculate respiration volume. Monitoring of the torso movement could also be done with depth sensors such as the Kinect, which creates a much high resolution map of the chest wall and abdomen.[65,66] Another method used to measure respiration volume is through transthoracic impedance which relates the change in impedance of the torso to respiration volume.[67] While all these methods can measure respiration volume, they can only operate in an immobile setting. Consequently, their use is limited to either a research or clinical setting and cannot monitor the patient in an ambulatory real-life setting.

Active, continuous, and wearable monitoring of patient vitals necessitates the monitor to be integrated seamlessly with their daily lives; this requires the monitors to be small, discrete and unobtrusive.[68–70] Accordingly, wearable respiration monitors have been developed that are smaller and more discrete. These sensors ranges from mechanical based capacitive and strain sensor measuring chest movement to acoustic based sensor listening to the flow of air in the trachea to air flow monitoring sensors placed under the nose.[71–75] However, these monitors can only measure respiration rate, and not volume. Researchers have developed an alternative wearable and remote RIP system that covers the patient's torso for measuring respiratory volume; however, this form factor is still bulky and cumbersome making application difficult. To the best of our knowledge, there has been no reported small discrete wearable respiratory sensor that can measure respiratory rate and respiratory volume.

7.3: Methods

7.3.1: Strain Sensor and Photoplethysmography Fabrication

The strain sensor fabrication protocol followed the protocol described in chapter 4.[43] Any sensors fabricated that had large variation in performance was discarded. A total of four sets of sensors were used for testing 8 subjects.

7.3.2: Hardware Setup

A wired acquisition system was used to measure the resistance change from the strain sensor. Figure 7.1 shows the diagram of the acquisition system. A multifunctional data acquisition system (Nation Instruments, USB-6003) was used to record the differential potential from the Wheatstone bridge configuration with one leg of the circuit connected to the strain sensor. All other elements of the circuit were 4.7 kΩ resistor elements. Continuous inhalation and exhalation flowrate were measured using a continuous spirometer (Vyaire, Vmax Encore 229). The system outputted the data as a voltage, which was then measured by the data acquisition system. A trip axis accelerometer was also used and measured from a second data acquisition system. An

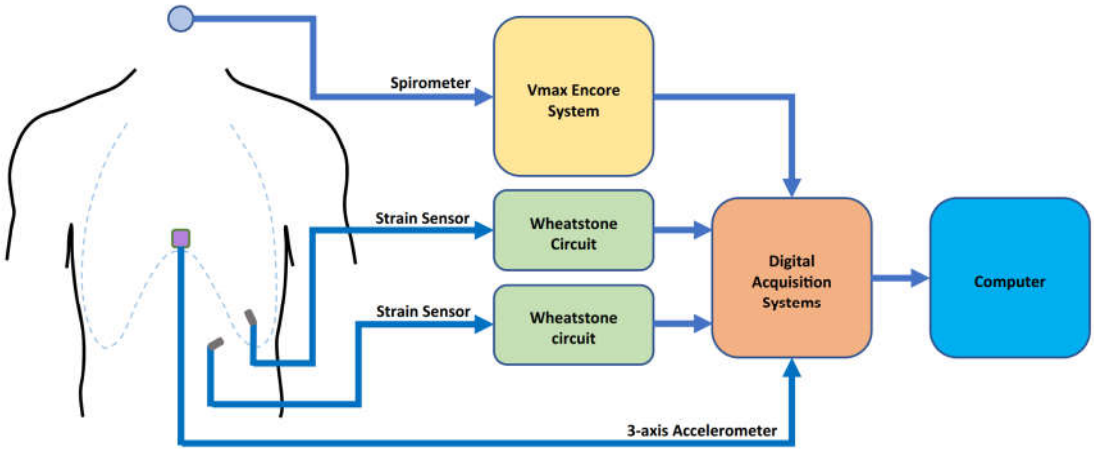

Figure 7.1. Diagram of the acquisition system used for measuring respiration and strain from the torso concurrently. The circle on the body is the continuous flow spirometer; the purple square is a 3-axis accelerometer; and the grey rectangles are the strain sensors.[44]

acquisition software (National Instrument, Signal Express 2015) was then used to acquire and sync all the data at a sample frequency of 1000 Hz.

7.3.3: Human Subject Testing Protocol

A total of 8 participants were tested under an approved study by the UC Irvine Institutional Review Board. Subject 1-7 were tested stationary in the reclined position, while subject 8 was tested under an ambulatory environment.

The height, weight, age, and sex of each subject was first recorded before testing. Afterwards, subject 1-7 was placed in a reclined position, and the two strain sensors was placed on their torso (figure 7.2). The first strain sensor was placed in the interstitial space between the 9^{th} and 10^{th} rib on the left side of the torso along the midclavicular line. The second strain sensor was placed in the upper left quadrant of the abdomen perpendicular to the first sensor, to minimize crosstalk. Each subject was asked to exhale fully before the sensors were placed. The accelerometer was placed right under the sternum with the x-axis and y-axis pointed towards the abdomen and towards the right side of the torso respectively; the z-axis was pointed into the body. Lastly, the spirometer was placed in the mouth, and secured in place using a head strap.

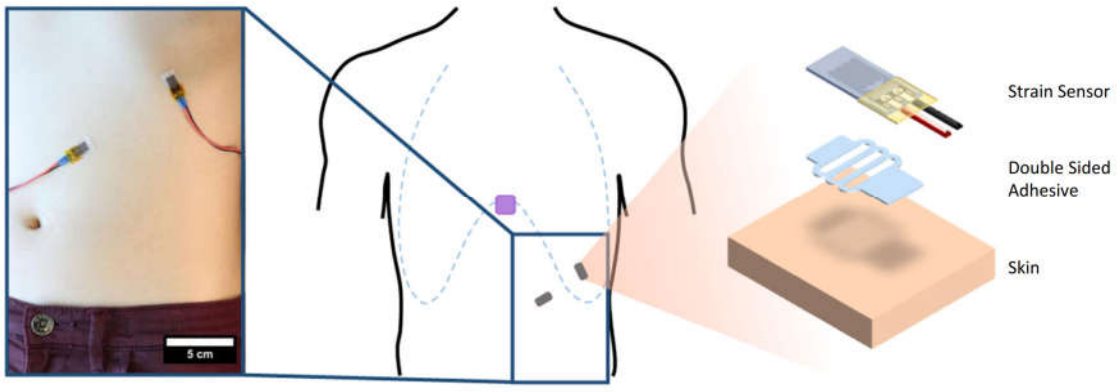

Figure 7.2. Placement of the strain sensor on the abdomen and ribcage perpendicular to each other. The sensors were adhered using double sided adhesive with strain relieving geometry cut into the adhesive.[44]

For the testing, the subject was first given 30 seconds to become acclimated to the testing set up. Afterwards, the subjects were asked to breath for 1 minutes each at 3 different respiration volume; they were asked to breath at a shallow, medium, and deep volume subject to their discretion. The data from the three different volumes was then used to build a calibration model for each subject to calculate respiration volume using the strain sensors. Next, the subject was asked to pace their breathing with an audio-visual metronome at three different rates. Breath rates of 10, 20, and 40 breaths per minute were performed for a period of 2 minutes, 1 minute, and 30 seconds respectively. After the paced breathing, the subject was asked to freely breath at different respiration volume in random order for 3 minutes. The data from this set will be used to confirm the calibration model created for each subject. Lastly, each subject was asked to perform 5 PFTs where they inhaled maximally and exhaled quickly and sharply, while sustaining their exhalation for 6 seconds; there was a 45 second break in between each maneuver. The top 3 PFTs were used according to ATS guidelines.[55]

The sensors placement for subject 8 was the same as subject 1-7. However, instead of laying in a reclined position, subject 8 was either standing or moving on a treadmill. The calibration procedure was performed while the subject was standing and walking at 4.8 km/h. The subject was then asked to pace his breathing at 20 breaths per minute while walking at 4.8 km/h. Afterwards, he was asked to breath freely for 3 minutes while still walking at 4.8 km/h. For the last test, the subject was asked to walk, jog, and run at 4.8, 9.7, and 12.9 km/h for 2 minutes at each speed.

7.3.4: Data Analysis

All data was processed using MATLAB (MathWorks, R2016b). The respiratory flow data measured using the Vmax system was first filtered to remove any large spikes in signal. Afterwards, the voltage was multiplied by a calibration constant of 2.04 l/sV to convert the voltage measurement into flowrate of liters per second. The continuous change in respiration volume was calculated by integrating the airflow with respect to time. Lastly, respiration volume was segmented between the inhalation and exhalation volume by integrating individual positive flow and negative flow segments. A cutoff volume of .01 l was used to remove any noise.

The calibration model for calculating volume using the strain sensor is a simple multiple linear regression based on work developed by Konno and Mead back in the late 1960s. The breath by breath exhalation volume and the associated change in resistance (ΔR) for the ribcage and abdomen was first extracted. A power regression model was then calculated and used to linearize the ΔR measured from the ribcage and abdomen sensor. Afterwards, multiple linear regression was used to develop a linear model between the data from the strain sensor and respiration volume. The ΔR from the strain sensor data for the free breathing was then linearized and inputted into the model to calculate respiration volume.

The paced breathing was analyzed by taking the average peak to peak interval between the strain sensors on the ribcage and abdomen for each frequency and comparing it to the peak to peak interval for the respiration waveform measured by the spirometer. A one-way analysis of variance (ANOVA) was used to determine if there was any significance between the calculated interval across the strain sensors and spirometer.

For the PFT, the calibration model was applied to the change in resistance of the strain sensor over time to calculate respiration volume. Afterwards, the forced expiratory volume at 1 second (FEV1) and forced vital capacity (FVC) was calculated. The forced expiatory volume percentage was also calculated (FEV1%)

For the measurement of respiration under motion, the dataset was first filtered using a low pass filter to remove any motion artifacts, which occurs at a higher frequency than breathing. Afterwards, the same data analysis done for the calibration model, free breathing, and respiration rate was performed. The frequency component of the signal was also examined for each type of walking or running speed.

7.4: Results and Discussion

7.4.1: Strain Sensor Characterization

The sensors used in this study are metal thin film crack-based strain sensors. The resistance of the sensor is increased via controlled cracking of the metal thin film layer. There are integrated micro- sized wrinkle structures that helps control the propagation of the cracking to prevent complete failure at smaller strain ranges. This allows the sensors to have a large operating range while maintaining sensitivity.

The sensors used in this study had a maximum range between 156% - 226%. They were cycled up to 2000 cycles without failure. The gauge factor for the sensors were between .85 to 2.64 when strained to 40% strain; the sensors performed relatively linearly, with R^2 values between .96 and 1 for a linear model. We hypothesize that the large variability in failure point and gauge factors within the strain sensors were from variations in manufacturing of each sensor. Because each sensor was built by hand, there will most likely be inconsistencies in the thin film. However, all measurement and calibration created was performed with respect to each individual sensor and person, so the variation between each sensor will be less impactful.

7.4.2: Respiratory Calibration Model

As previously described, the strain sensors were placed on the abdomen and ribcage of the subjects. The sensors have a dimension of 21 mm by 10 mm by .5 mm and was placed perpendicularly to each other to minimize any crosstalk in data. A double-sided FDA approved adhesive was used to adhere the sensors onto the skin. Curved strain relief patterns were laser cut into the tape to allow the adhesive to stretch and move with the sensor. The strain relief

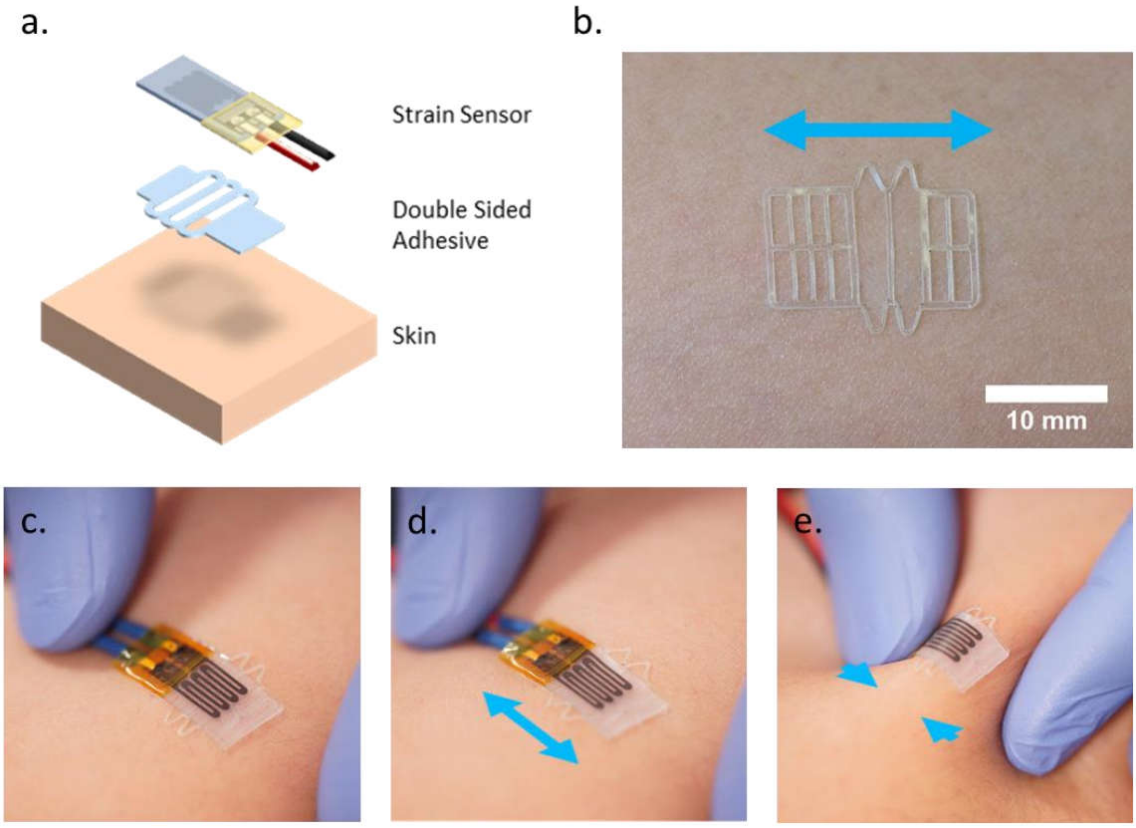

Figure 7.3. (a) An exploded diagram showing how the strain sensors were placed on the skin. (b) A picture of the actual adhesive used to adhere the sensor on to the skin. The arrow marks the direction of the strain. (c-e) The strain sensor unstretched, under tension and under compression.[44]

pattern had a single strip of adhesive running perpendicular to the length of the sensor to prevent the center of the sensor from lifting off (figure 7.3).

There were 8 participants in this study. All participants were healthy individual with no active respiratory problems. Subject 1 had moderately severe childhood asthma but no symptoms were present during the study. There were 3 female and 5 male participants. The average height, weight, and BMI were respectively 172 cm with a standard deviation of 8 cm, 65 kg with a standard deviation of 10 kg, and 22 kg/m^2 with a standard deviation of 2 kg/m^2.

For the calibration model, each subject was asked to breath at a shallow, medium, and deep respiration volume at their discretion. Afterwards the exhalation volume and associated

change in resistance (ΔR) from the strain sensors were calculated. The majority of the data, between the individual sensor ΔR and exhalation volume (V), followed a power regression model for all subjects:

$$V = a\Delta R^b$$

Where a and b are constants. Separate power models were created for ΔR from the ribcage and abdomen sensors. This model was used to linearize the ΔR from both strain sensors before a multiple linear regression (MLR) model was used to correlate the strain sensors output with exhalation volume. The model used was:

$$V = a + b\Delta R^*_{Abd} + c\Delta R^*_{Rib}$$

Where a, b, and c are constants and ΔR^*_{Abd} and ΔR^*_{Rib} are the linearized outputs from the abdomen and ribcage strain sensors respectively, and V is the respiration volume. The linearized

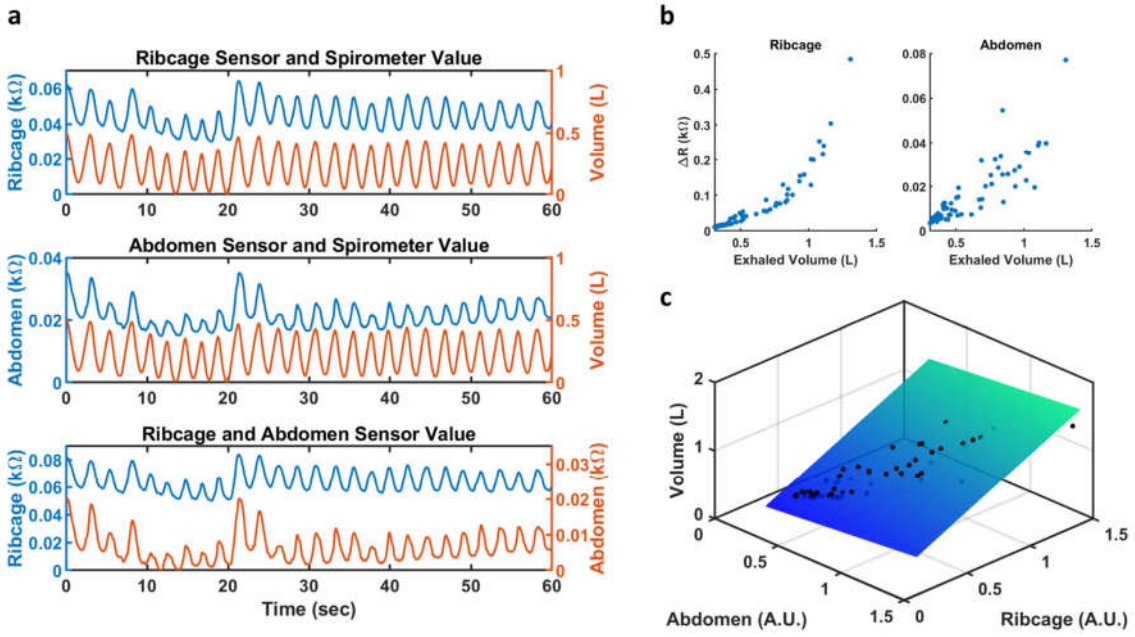

Figure 7.4. (a) Waveforms from the strain sensors placed on the abdomen and ribcage as well as the concurrent respiration volume measured over time. (b) Scatterplots of the exhalation volume plotted against the associated change in resistance. (c) A 3D scatterplot of the linearized data from the abdomen and ribcage strain sensor plotted against exhalation volume.[44]

Table 7.1[44]

		Power Regression (Ribcage)		Power Regression (Abdomen)		MLR (Ribcage + Abdomen)	
Subject	**Sex**	R^2	**SEE**	R^2	**SEE**	R^2	**SEE**
1	Male	0.92	0.122	0.87	0.151	0.93	0.111
2	Male	0.83	0.2	0.9	0.15	0.96	0.098
3	Female	0.91	0.226	0.67	0.426	0.92	0.213
4	Female	0.97	0.173	0.76	0.462	0.97	0.166
5	Male	0.83	0.236	0.94	0.136	0.94	0.136
6	Female	0.96	0.054	0.8	0.12	0.96	0.051
7	Male	0.95	0.166	0.94	0.186	0.97	0.139

ΔR was then used in the MLR model to find a best fit plane between the linearized data from the strain sensor and respiration volume (figure 7.4). The R^2 values for the MLR was relatively high. Table 7.1 gives the R^2 values for each model as well as the standard error estimation.

Overall, there seems to be more variation in ΔR compared for the abdomen compared to the ribcage. However, this variation is accounted for by the MLR, which had an overall improved fit between the transformed ΔR. This follows the concept first proposed by Konno and Mead, where a linear model could be used to correlate movement of the chest wall and abdomen to respiration volume. It should be noted that for every subject, one of the two power models could already model the majority of the exhalation volume. This would suggest that respiration is predominantly performed by one mechanism. However, the mechanism each person used to breath, whether through the ribcage or abdomen, is different, so having sensors placed at both locations is still needed to create a comprehensive and robust model.

7.4.3: Calculating Respiration Rate and Respiration Volume

The respiration volume for each subject was calculated using the power models and MLR model developed using the calibration data set. The subjects were asked to breath at random volumes varying from shallow to deep. The signals from the abdomen was then taken, and exhalation volume and associated ΔR was calculated. The data was then linearized using the power model and inputted into the MLR to calculate respiration volume.

Figure 7.5a shows the scatter plot of the calculated exhalation volume plotted against the measured exhalation volume for all subjects. Figure 7.5b shows the bland Altman from the same set of data. The Bland Altman had a bias of 0.077 l with limits of agreements (LoAs) of -.374 l and .220l. The Lin's concordance correlation coefficient showed substantial agreement between the calculated and measured respiration volume with a value of .962. There was only moderate agreement between the calculated inhalation volume and measure inhalation volume, with a

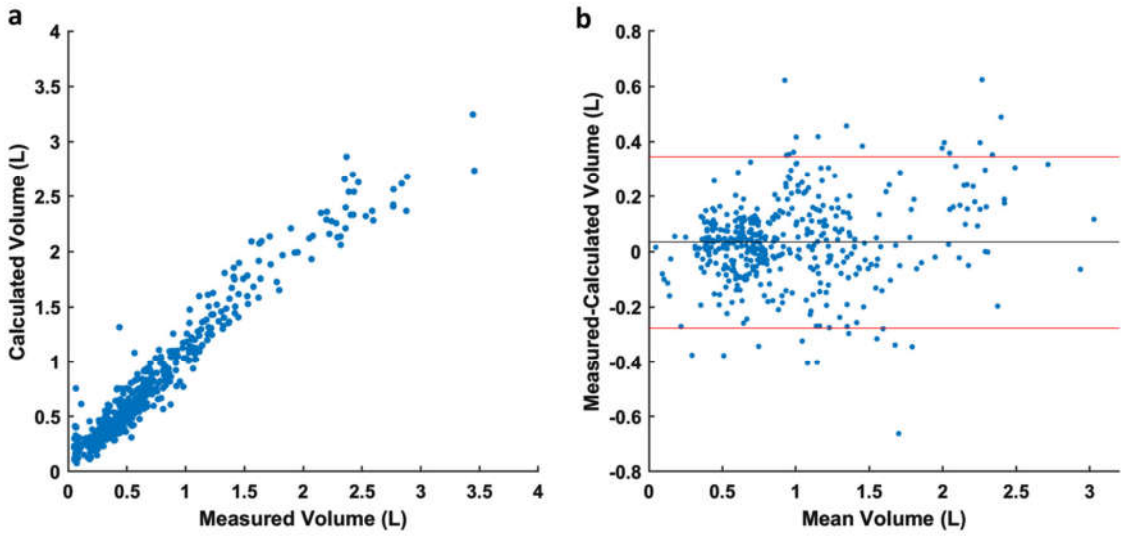

Figure 7.5. (a) The scatterplot of the calculated volume versus the measured volume. (b) The Bland Altman for the calculated versus measured volume.[44]

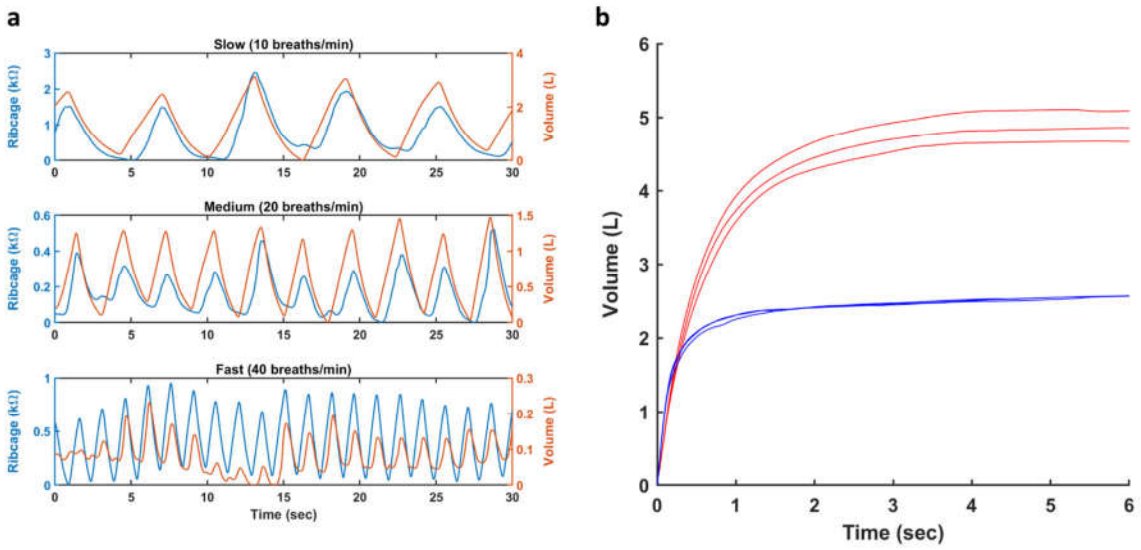

Figure 7.6. (a) Respiration waveform plotted with the ribcage strain sensor waveform. (b) The PFT volume calculated over time from the strain sensor plotted with the measured volume for the PFT.[44]

concordance correlation coefficient of .929. This was most likely due to hysteresis within the sensor.

Respiration rate was measured by calculating the peak to peak period for each breath for both the strain sensor signal and the respiration measured from the continuous spirometer. Each subject was asked to pace their respiration with a metronome at 10, 20, and 40 breaths per minute. Figure 7.6a shows a representative waveform of a detrended paced breathing. The average of each rate was then calculated. A one-way analysis of variance (ANOVA) showed no significant differences across the abdomen strain sensor, ribcage strain sensor, and the spirometer for each respiration rate for all subjects.

Overall, we demonstrated that the strain sensors were able to calculate respiration rate and volume with good agreement under sedentary conditions. While most systems used in literature requires measurements to be made over large area, our system demonstrates that

respiration volume and rate could still be calculated using a smaller area of the abdomen and ribcage.

7.4.4: Pulmonary Function Test

The pulmonary function test consists of a completely and deep inhalation followed by a quick and immediate exhalation. The maneuver was performed 5 times by the subject, and the top 3 maneuvers were used, according to the ATS standard. The calibration model was applied to the ΔR of the strain sensor during the maneuver, and the forced expiratory volume at one second (FEV1), forced vital capacity (FVC), and ratio of FEV1 to FVC (FEV1%) was calculated for both the strain sensor and spirometer data. Figure 7.6b shows representative data from one subject. Across all subjects, the calculated FEV1 and FVC values were lower compared to the measured values. However, the calculated FEV1% were closer to the measured FEV1%, although it was not statistically significant.

The PFT demonstrates the shortcoming of the system. There is an inherent hysteresis with elastomeric based sensors, we hypothesize that this hysteresis is more prominent with high rate, high amplitude motion, like the PFT. For normal respiration, like the protocol performed before the PFT, the breathing action is smaller and slower. Thus, the hysteresis was minimal, and could be accounted for post-processing. Conversely, the inhalation and exhalation action of the PFT did not allow the sensor to return to its initial baseline in time. This resulted in a measured ΔR that was smaller which resulted in a calculated volume that was lower. This type of hysteresis is not unique to this system, most elastomeric system will have some form of hysteresis due to the viscoelastic nature of the polymer. This needs to be accounted for or minimized, especially for maneuvers that requires fast and high amplitude actions.

7.4.5: Measuring Respiration Under Motion

Subject 8 repeated all the respiration maneuver subjects 1-7 performed, apart from the PFT. The calibration protocol and free breathing protocol was performed while walking at 4.8 km/h. The subject was also asked to pace his breathing at 20 breaths per minute.

As the subject went from stationary to ambulatory, his respiration volume started to increase; this is the body's natural response to meet the increase oxygen consumption. This increase in respiration volume was also captured by the strain sensors (Figure 7.7a-b). While the subject was ambulatory, there is clear artifacts in the strain signals due to the motion. The motion artifacts present itself as periodic waveforms that occurs at a higher frequency compared to the respiration rate (figure 7.7c). A low pass filter was used to remove the motion artifacts before

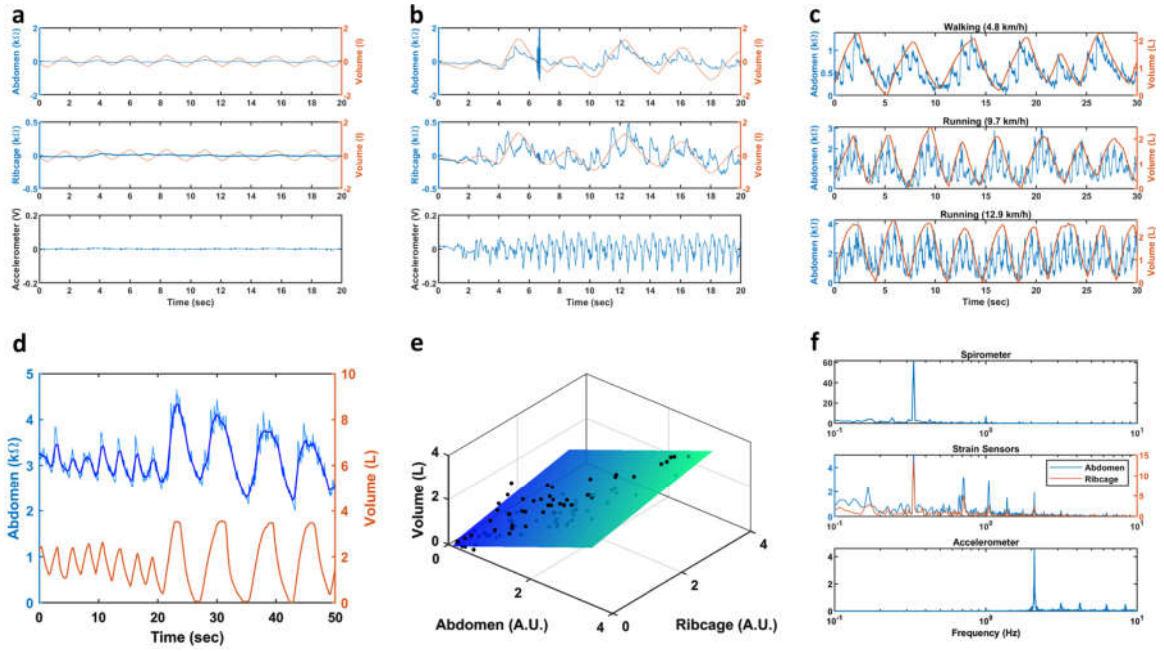

Figure 7.7. (a-b) Plots of the respiration volume, strain sensor output from the abdomen and ribcage, and accelerometer for the stationary subject and subject under motion. (c) Plots of the abdomen sensor output and the respiration volume for the walking, jogging, and running pace. (d) Plot of the strain sensor data (light blue) and the filtered data (dark blue). The respiration volume is plotted underneath. (e) Scatter plot and best fit plane of the linearized data plotting against volume. (f) Plots of the frequency decomposition of the respiration, strain sensor, and accelerometer signal under paced breathing while walking.[44]

the respiration volume and associated ΔR was calculated, and the calibration model was created (figure 7.7d). The power model had an R^2 value of .8 and .62 respectively for the strain sensors on the abdomen and the ribcage. The adjusted R^2 value for the MLR had a value of .83. While this indicates that the MLR model during walking has a poorer fit compared to the stationary model, this should be expected since there are significantly more motion artifacts present in the signal that needs to be filtered out (figure 7.7e). While the model fit was acceptable, the calculated respiration volume from the free breathing had a poor fit with a Lin's concordance correlation calculated was .75.

The respiration rate was calculated as described for the stationary subjects. To prevent too much strain on the subject, only a single respiration rate at 20 breaths per minute was performed. There was no significant difference between the respiration calculated by the spirometer and strain sensor (p=.9935). Interestingly, there frequency decomposition of the strain sensor signal, accelerometer, and spirometer signal shows overlapping frequencies. Specifically, the strain sensors seem to contain frequencies that are in both the spirometer and the accelerometer. There is an overlapping peak at .333 Hz between the spirometer and strain sensor which corresponds to the paced breathing rate. The strain sensor and y-component of the accelerometer also has an overlapping peak at 2.09 Hz, which is assumed to be from the gait motion of walking (figure 7.7f).

As the subject transitioned from walking to jogging and then to walking, the relative respiration volume amplitude did not change significantly. When examined qualitatively, there is an apparent growth in the amplitude of the motion artifact in the strain sensor. However, despite the increase in noise from the motion artifact, there is still a visible trend in the strain sensor data

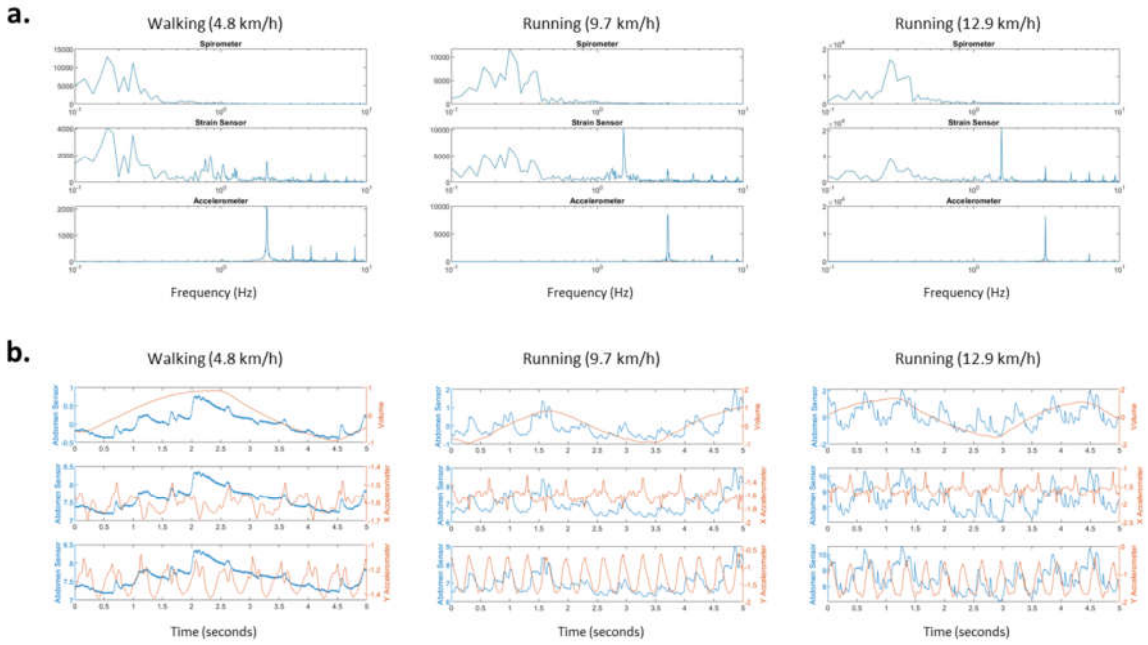

Figure 7.8. (a) Frequency decomposition of the spirometer, strain sensor, and accelerometer for walking and the two different running paces. (b) Plots of the waveform over time for the same conditions listed in (a).[44]

that matches the respiration volume. In the frequency decomposition of the respiration, strain sensor, and accelerometer signal, there is an overlapping cluster of frequencies that should be associated with breathing in the spirometer and strain sensor signal. There is also overlapping frequencies between the accelerometer and the strain sensors. However, as the running pace increases, there is an additional frequency in the strain sensor signal that is not accounted for in either the accelerometer or respiration volume (figure 7.8). Once the subject started running, frequencies of 1.52 and 1.55 Hz appeared in the strain sensor signal for the 9.7 and 12.9 km/h pace respectively. The dominant frequency in the accelerometer was 3.05 and 3.10 Hz respectively for the 9.7 and 12.9 km/h pace. This frequency may be a result of the body torsion that occurs for every two steps during running.

Overall, we demonstrated that it is possible to get a preliminary calibration model for respiration with movement. However, there was poor agreement between the calculated respiration volume and measured respiration volume. The respiration rate was measured accurately after proper filtering despite the increased motion artifacts compared to non-ambulatory patients. Even at faster running pace, there was still a visual trend between the respiration volume and the strain sensor data. With improved filtering, it may be possible to calculate respiration volume with higher accuracy during periodic motions.

7.5: Conclusion

7.5.1: Summary

We demonstrated that respiration volume could be calculated with a stationary subject by measuring the strain over a small footprint of the torso and abdomen using soft, stretchable strain sensors. Respiration rate and volume could be accurately calculated in subjects who are laying in the supine position. Moreover, a calibration model was also created for a single subject under ambulatory conditions. Due to the limitation of the sensors, PFT was not accurately captured; however, we believe a relative change in the PFT could be captured.

7.5.2: Future Works

The study shown in this chapter demonstrate the capabilities of flexible electronics fabricated using a low cost and rapid manufacturing method. Future work needs to be focused on optimizing the system for a more ambulatory and less controlled environment outside of a clinical environment or a research lab. Other challenges include creating a good motion artifact filtering or rejection scheme that guarantees the signal acquired is high quality. Moreover, other sensors could be integrated, such as ECG, to provide more information that can be used to monitor a variety of different disease, and not just respiratory based diseases.

Chapter 8: Discussion and Future Prospect

8.1: Summary

Application of wearable sensors for monitoring human vitals have different requirements stemming from patient and hardware considerations. From the sensor perspective, the entire system must be soft and conformal to the skin. This requirement is not just motivated by human comfort, but also is necessary for acquiring high fidelity signals. From the patient side, a good understanding of the human body is necessary to know the type and quality of signal that can be extracted from the body. In this work, we hope to have demonstrated preliminary work in each of these compartments that will hopefully evolve into a comprehensive system for monitoring human vitals.

In chapter 5, we demonstrated a low cost and simple method for fabricating Microfluidic devices that can potentially be integrated towards making wearable point of care systems. This method uses a novel silicone-based polymer mixture that can create reversible or irreversible bonds with glass and PDMS respectively. This process is not acutely time sensitive and does not require any capital equipment making fabrication easier and simpler.

In chapter 6, a process was explored for integrating conventional SMD with a flexible and stretchable substrate. A method for controlling the distribution of strain through the substrate was described using strain relieving islands with “cove” geometries. The cove structures prevent any large formation of strain at the interface between the interconnect and the island mesh. High strains at these interfaces normally leads to early mechanical failure of the device. Using this technique, different circuits were constructed, and their functions were demonstrated during strain. Pulse rate was also measured using an integrated system that combined PPG technology

with the strain sensor used for measuring respiration. The system was demonstrated to be able to measure respiration and pulse concurrently.

Chapter 7 describes how we applied and optimized a system for measuring respiration volume and rate in humans. Two highly flexible and stretchable strain sensors were applied to the chest wall and abdomen of the torso. The exhalation and inhalation volume were then correlated with the change in signal from the strain sensor to create a model for calculating volume. Successful application of this system for measuring respiration volume and rate was demonstrated.

8.2: Future Works

Much of the work done in this dissertation demonstrates initial proof of concept for different areas in wearable technology. Accordingly, there are many different directions for future works.

We demonstrated initial proof of concept for creating a highly stretchable and flexible system that integrates traditional SMD and with stretchable electronics. While we did show different types of circuits, the system was still missing several very important components. The first component was the power source and the second components missing were the microcontroller and wireless communication system. The next step in this project would be to start integrating these components in a flexible circuit; this would create a truly flexible and stretchable system with minimal hard components. Further down the line, a soft flexible circuit could then be created and potentially combined with wearable microfluidic for a wireless wearable electrochemical testing.

The work done for monitoring respiration was only in stationary environments. For a wearable system to be truly ubiquitous, it should operate in different environments, including ambulatory environments. Thus, different schemes for filtering and removing motion artifacts with the strain sensors should be explored. This could include having a second sensor to serve as a comparison point to filter out common artifacts. The respiration sensors could also be applied in different disease populations to determine how the signal is different between a healthy and diseased population. A good example is capturing potential asthma attacks in asthmatic patients. This could be accomplished by placing the sensors on patients who are undergoing diagnosis with the methacholine challenge. This diagnostic test induces asthma in patients who are hypersensitive to the methacholine drug. Understanding the changes in the respiration waveform could help inform future machine learning algorithm for predicting the onset of asthma.

8.3: Future Prospects

For wearable technology to be truly ubiquitous in the future, there are several challenges that must be addressed. There are very few soft electronic systems that does not require integration with a traditional PCB to be connected with the current wireless infrastructure. Soft electronic Systems that have demonstrated successful integration typically has a very complex fabrication process that makes scaling difficult. For soft, wearable sensors to be widespread, there needs to first be a method that can both integrate all the important component for a circuit, including battery, microcontroller, and wireless antenna. The second important requirement is for this process to be scalable. The fabrication method used in this dissertation has the potential to be scalable in the roll to roll process. Without a good manufacturing plan, soft, wearable

devices will largely remain in the academic realm. Lastly, the data that's acquire must be high quality and actionable. This means that schemes for eliminating motion artifacts, or identify, poor quality data must be developed. High quality data can then be fed into machine algorithm schemes to help identify irregular signals and potentially help diagnose patients. The eventual widespread application of wearable systems, in conjunction with strong data processing, can create a system that can improve the quality of life for patients and improve medicine itself.

References

1. Kostopoulou, O., Delaney, B. C. & Munro, C. W. Diagnostic difficulty and error in primary care - A systematic review. *Fam. Pract.* **25**, 400–413 (2008).
2. Asher, I. & Pearce, N. Global burden of asthma among children. *Int. J. Tuberc. Lung Dis.* **18**, 1269–1278 (2014).
3. Tomasic, I., Tomasic, N., Trobec, R., Krpan, M. & Kelava, T. Continuous remote monitoring of COPD patients—justification and explanation of the requirements and a survey of the available technologies. *Medical and Biological Engineering and Computing* **56**, 547–569 (2018).
4. Bui, A. L. & Fonarow, G. C. Home monitoring for heart failure management. *Journal of the American College of Cardiology* **59**, 97–104 (2012).
5. Rodbard, D. Continuous Glucose Monitoring: A Review of Successes, Challenges, and Opportunities. *Diabetes Technology and Therapeutics* **18**, S23–S213 (2016).
6. Vishal Nangalia, David R Prytherch, G. B. S. *Health technology assessment review: Remote monitoring of vital signs - current status and future challenges*. (2010).
7. Yamada, T. *et al.* A stretchable carbon nanotube strain sensor for human-motion detection. (2011). doi:10.1038/NNANO.2011.36
8. Heikenfeld, J. *et al.* Wearable sensors: Modalities, challenges, and prospects. *Lab Chip* **18**, 217–248 (2018).
9. Heikenfeld, J. *et al.* Wearable sensors: Modalities, challenges, and prospects. *Lab Chip* **18**, 217–248 (2018).
10. Ash, C., Dubec, M., Donne, K. & Bashford, T. Effect of wavelength and beam width on

penetration in light-tissue interaction using computational methods. *Lasers Med. Sci.* **32**, 1909–1918 (2017).

11. Bandodkar, A. J., Jeang, W. J., Ghaffari, R. & Rogers, J. A. Annual Review of Analytical Chemistry Wearable Sensors for Biochemical Sweat Analysis. *Annu. Rev. Anal. Chem. 2019* **12**, 1–22 (2019).
12. Overview of the Cardiovascular System | Cardiovascular Physiology, 9e | AccessMedicine | McGraw-Hill Medical. Available at: https://accessmedicine.mhmedical.com/content.aspx?sectionid=190800340&bookid=2432&Resultclick=2#1153945990. (Accessed: 5th November 2019)
13. Tison, G. H. *et al.* Passive detection of atrial fibrillation using a commercially available smartwatch. *JAMA Cardiol.* **3**, 409–416 (2018).
14. Chapter 1. Function and Structure of the Respiratory System | Pulmonary Physiology, 8e | AccessMedicine | McGraw-Hill Medical. Available at: https://accessmedicine.mhmedical.com/content.aspx?bookid=575&sectionid=42512979. (Accessed: 5th November 2019)
15. Joodaki, H. & Panzer, M. B. Skin mechanical properties and modeling: A review. *Proc. Inst. Mech. Eng. Part H J. Eng. Med.* **232**, 323–343 (2018).
16. Kim, D. H. *et al.* Epidermal electronics. *Science (80-.).* **333**, 838–843 (2011).
17. Arumugam, V. & Sanjeevi, R. *Effect of strain rate on the fracture behaviour of skin*. *J. Biosci* **19**, (1994).
18. Konno, K. & Mead, J. Measurement of the separate volume changes of rib cage and abdomen during breathing. *J. Appl. Physiol.* **22**, 407–22 (1967).

19. Lee, J. B. & Khang, D. Y. Electrical and mechanical characterization of stretchable multi-walled carbon nanotubes/polydimethylsiloxane elastomeric composite conductors. *Compos. Sci. Technol.* **72**, 1257–1263 (2012).

20. Larmagnac, A., Eggenberger, S., Janossy, H. & Vörös, J. Stretchable electronics based on Ag-PDMS composites. (2014). doi:10.1038/srep07254

21. Kaur, G., Adhikari, R., Cass, P., Bown, M. & Gunatillake, P. Electrically conductive polymers and composites for biomedical applications. (2015). doi:10.1039/c5ra01851j

22. Xu, F. & Zhu, Y. Highly Conductive and Stretchable Silver Nanowire Conductors. *Adv. Mater.* **24**, 5117–5122 (2012).

23. Kayser, L. V. & Lipomi, D. J. Stretchable Conductive Polymers and Composites Based on PEDOT and PEDOT:PSS. *Adv. Mater.* **31**, 1806133 (2019).

24. Wang, Y. *et al.* A highly stretchable, transparent, and conductive polymer. *Sci. Adv.* **3**, (2017).

25. Boley, J. W., White, E. L., Chiu, G. T.-C. & Kramer, R. K. Direct Writing of Gallium-Indium Alloy for Stretchable Electronics. *Adv. Funct. Mater.* **24**, 3501–3507 (2014).

26. Tabatabai, A., Fassler, A., Usiak, C. & Majidi, C. Liquid-Phase Gallium–Indium Alloy Electronics with Microcontact Printing. *Langmuir* **29**, 6194–6200 (2013).

27. Kramer, R. K., Majidi, C. & Wood, R. J. Masked Deposition of Gallium-Indium Alloys for Liquid-Embedded Elastomer Conductors. *Adv. Funct. Mater.* **23**, 5292–5296 (2013).

28. Robinson, A., Aziz, A., Liu, Q., Suo, Z. & Lacour, S. P. Hybrid stretchable circuits on silicone substrate. *J. Appl. Phys.* **115**, (2014).

29. Fan, J. A. *et al.* ARTICLE Fractal design concepts for stretchable electronics. *Nat. Commun.*

(2014). doi:10.1038/ncomms4266. This work is licensed under a Creative Commons Attribution 4.0 International License.

30. Yeo, W.-H. *et al.* Multifunctional Epidermal Electronics Printed Directly Onto the Skin. *Adv. Mater.* **25**, 2773–2778 (2013).

31. Lacour, S. P., Jones, J., Suo, Z. & Wagner, S. Design and performance of thin metal film interconnects for skin-like electronic circuits. *IEEE Electron Device Letters* **25**, 179–181 (2004).

32. Lacour, S. P., Jones, J., Wagner, S., Li, T. & Suo, Z. Stretchable Interconnects for Elastic Electronic Surfaces. *Proceedings of the IEEE* **93**, 1459–1466 (2005).

33. Lacour, S. P., Wagner, S., Huang, Z. & Suo, Z. Stretchable gold conductors on elastomeric substrates. *Appl. Phys. Lett.* **82**, 2404–2406 (2003).

34. Harris, K. D., Elias, A. L. & Chung, H. J. Flexible electronics under strain: a review of mechanical characterization and durability enhancement strategies. *Journal of Materials Science* **51**, 2771–2805 (2016).

35. Suo, Z. Mechanics of stretchable electronics and soft machines. *MRS Bull.* **37**, 218–225 (2012).

36. Xu, S. *et al.* Soft microfluidic assemblies of sensors, circuits, and radios for the skin. *Science (80-.).* **344**, 70–74 (2014).

37. Huang, Z. *et al.* Three-dimensional integrated stretchable electronics. *Nat. Electron.* **1**, 473–480 (2018).

38. Lu, T., Markvicka, E. J., Jin, Y. & Majidi, C. Soft-Matter Printed Circuit Board with UV Laser Micropatterning. *ACS Appl. Mater. Interfaces* **9**, 22055–22062 (2017).

39. Moser, R. *et al.* From playroom to lab: Tough stretchable electronics analyzed with a tabletop tensile tester made from toy-bricks. *Adv. Sci.* **3**, 1–9 (2016).

40. Romeo, A., Liu, Q., Suo, Z. & Lacour, S. P. Elastomeric substrates with embedded stiff platforms for stretchable electronics. *Appl. Phys. Lett.* **102**, (2013).

41. Nokes, J. M. *et al.* Reduced Blood Coagulation on Roll-to-Roll, Shrink-Induced Superhydrophobic Plastics. *Adv. Healthc. Mater.* **5**, 593–601 (2016).

42. Kim, J. *et al.* Highly stretchable wrinkled gold thin film wires. *Appl. Phys. Lett.* **108**, (2016).

43. Pegan, J. D. *et al.* Skin-mountable stretch sensor for wearable health monitoring †. **8**, 17295 (2016).

44. Chu, M. *et al.* Respiration rate and volume measurements using wearable strain sensors. *npj Digit. Med.* **2**, (2019). This work is licensed under a Creative Commons Attribution 4.0 International License.

45. Park, S.-J., Kim, J., Chu, M. & Khine, M. Highly Flexible Wrinkled Carbon Nanotube Thin Film Strain Sensor to Monitor Human Movement. *Adv. Mater. Technol.* **1**, 1600053 (2016).

46. Koh, A. *et al.* A soft, wearable microfluidic device for the capture, storage, and colorimetric sensing of sweat. *Sci. Transl. Med.* **8**, (2016).

47. Chu, M., Nguyen, T. T., Lee, E. K., Morival, J. L. & Khine, M. Plasma free reversible and irreversible microfluidic bonding. *Lab Chip* **17**, 267–273 (2017).

48. Lee, S. M. *et al.* Self-adhesive epidermal carbon nanotube electronics for tether-free long-term continuous recording of biosignals. *Sci. Rep.* **4**, (2014).

49. Raghupathi, W. & Raghupathi, V. An empirical study of chronic diseases in the united

states: A visual analytics approach. *Int. J. Environ. Res. Public Health* **15**, (2018).

50. Ferkol, T. & Schraufnagel, D. The Global Burden of Respiratory Disease. *Ann. Am. Thorac. Soc.* **11**, 404–406 (2014).

51. Nurmagambetov, T., Kuwahara, R. & Garbe, P. The Economic Burden of Asthma in the United States, 2008–2013. *Ann. Am. Thorac. Soc.* **15**, 348–356 (2018).

52. Guarascio, A. J., Ray, S. M., Finch, C. K. & Self, T. H. ClinicoEconomics and Outcomes Research The clinical and economic burden of chronic obstructive pulmonary disease in the USA. *Clin. Outcomes Res.* 5–235 (2013). doi:10.2147/CEOR.S34321

53. Nelson, S., Whitsel, L., Khavjou, O., Phelps, D. & Leib, A. *Prepared for*. (2016).

54. Crapo, R. O. Pulmonary-Function Testing. *N. Engl. J. Med.* **331**, 25–30 (1994).

55. Miller, M. R. *et al.* Standardisation of spirometry. doi:10.1183/09031936.05.00034805

56. Criée, C. P. *et al.* Body plethysmography – Its principles and clinical use. *Respir. Med.* **105**, 959–971 (2011).

57. Hmeidi, H. *et al.* Tidal breathing parameters measured using structured light plethysmography in healthy children and those with asthma before and after bronchodilator. *Physiol. Rep.* **5**, e13168 (2017).

58. Dall'Ava-Santucci, J. & Armanganidis, A. Respiratory Inductive Plethysmography. in *Pulmonary Function in Mechanically Ventilated Patients* 121–142 (Springer, Berlin, Heidelberg, 1991). doi:10.1007/978-3-642-84209-2_11

59. Sackner, M. A. *et al.* Calibration of respiratory inductive plethysmograph during natural breathing. *J. Appl. Physiol.* **66**, 410–20 (1989).

60. Collop, N. A. *et al.* Clinical guidelines for the use of unattended portable monitors in the

diagnosis of obstructive sleep apnea in adult patients. Portable Monitoring Task Force of the American Academy of Sleep Medicine. *J. Clin. Sleep Med.* **3**, 737–47 (2007).

61. Cantineau, J. P., Escourrou, P., Sartene, R., Gaultier, C. & Goldman, M. Accuracy of Respiratory Inductive Plethysmography during Wakefulness and Sleep in Patients with Obstructive Sleep Apnea. *Chest* **102**, 1145–1151 (1992).

62. Farré, R., Montserrat, J. M. & Navajas, D. Noninvasive monitoring of respiratory mechanics during sleep. doi:10.1183/09031936.04.00072304

63. Massaroni, C. *et al.* Optoelectronic Plethysmography in Clinical Practice and Research: A Review. *Respiration.* **93**, 339–354 (2017).

64. ALIVERTI, A. *et al.* Optoelectronic Plethysmography in Intensive Care Patients. *Am. J. Respir. Crit. Care Med.* **161**, 1546–1552 (2000).

65. Aoki, H. *et al.* Non-contact respiration measurement using structured light 3-D sensor. *SICE Annu. Conf.* 614–618 (2012).

66. Soleimani, V. *et al.* Depth-based Whole Body Photoplethysmography in Remote Pulmonary Function Testing. *IEEE Trans. Biomed. Eng.* **65**, 1421–1431 (2017).

67. Voscopoulos, C. *et al.* Evaluation of a Novel Noninvasive Respiration Monitor Providing Continuous Measurement of Minute Ventilation in Ambulatory Subjects in a Variety of Clinical Scenarios. *Anesth. Analg.* **117**, 91–100 (2013).

68. Yilmaz, T. *et al.* Detecting Vital Signs with Wearable Wireless Sensors. *Sensors* **10**, 10837–10862 (2010).

69. Khan, Y., Ostfeld, A. E., Lochner, C. M., Pierre, A. & Arias, A. C. Monitoring of Vital Signs with Flexible and Wearable Medical Devices. *Adv. Mater.* **28**, 4373–4395 (2016).

70. Patel, S., Park, H., Bonato, P., Chan, L. & Rodgers, M. A review of wearable sensors and systems with application in rehabilitation. *J. Neuroeng. Rehabil.* **9**, 21 (2012).

71. Wang, Y. *et al.* Wearable and Highly Sensitive Graphene Strain Sensors for Human Motion Monitoring. *Adv. Funct. Mater.* **24**, 4666–4670 (2014).

72. Laukhina, E. *et al.* Ultrasensitive Piezoresistive All-Organic Flexible Thin Films. *Adv. Mater.* **22**, 977–981 (2010).

73. Li, Y., Samad, Y. A. & Liao, K. From cotton to wearable pressure sensor. *J. Mater. Chem. A* **3**, 2181–2187 (2015).

74. Mimoz, O., Benard, T., Gaucher, A., Frasca, D. & Debaene, B. Accuracy of respiratory rate monitoring using a non-invasive acoustic method after general anaesthesia. *Br. J. Anaesth.* **108**, 872–875 (2012).

75. AL-Khalidi, F. Q., Saatchi, R., Burke, D., Elphick, H. & Tan, S. Respiration rate monitoring methods: A review. *Pediatr. Pulmonol.* **46**, 523–529 (2011).